Omnisoot: an object-oriented computational package for the simulation of the gas phase synthesis of Carbon Black

Mohammad Adib[*], Sina Kazemi[1], M. Reza Kholghy[1, †]

Abstract

A computational tool, *omnisoot* was developed based on chemical kinetic functionalities of Cantera to describe formation of carbonaceous nanoparticles such as soot and Carbon Black (CB) from reaction of gaseous hydrocarbons. Four reactor models built in the tool can provide a simplified description of complex industrial processes. Omnisoot couples gas chemistry with the soot model that entails two different aerosol dynamics models, and four inception and surface growth models from the literature, which makes it a robust tool for analyzing particle yield and morphology in various experimental targets such as shock-tubes, and flow and well-stirred reactors. The integrated architecture of omnisoot enables highlighting the uncertainty in soot modelling that originates from gas chemistry and elucidating the difference between inception models in short and long residence times in the presence of active inception and surface growth and end of them. The temperature dependence of inception model significantly affects the particle size distribution measured at the end of a pyrolysis flow reactor where only irreversible models seem to predict the bimodality. The tool also provides essential information about the contribution of inception and surface growth to total soot mass as a determining factor in soot morphology. For example, in shock-tube pyrolysis of methane multiple combinations of inception and surface growth can minimize the prediction of carbon yield, but lead to remarkably different morphologies, which emphasizes the need for characterization of soot morphology to constrain inception and surface growth fluxes.

[*]Department of Mechanical and Aerospace Engineering, Carleton University, 1125 Colonel By Dr, Ottawa, ON K1S 5B6, Canada

[†]Correspondeing author

1 Introduction

The formation of carbonaceous nanoparticles such as soot and Carbon Black (CB) is a complex and multi-scale process that involves chemical reactions, heat transfer, fluid and particle dynamics and spans over wide length ($\sim 10^{-12}$ to 1 m) and time ($\sim 10^{-15}$ to 1 s) scales. Understanding the effect of process parameters on particle concentration, morphology, and composition is not trivial, but crucial due to health and environmental impacts of soot and functional properties of CB. Soot is a broad-band light absorbers [1], and is emitted in large scales ($\approx$9.5 megatons of soot) acting as the third strongest contributor to climate change after methane and carbon dioxide [2]. Its fine particulate nature ($PM_{2.5}$) also raises health concerns [3]. In contrast, CB, the largest flame-made nanomaterial by production volume ($\sim$15 megatons annually), plays a critical role in industrial applications, including rubber reinforcement [4] and lithium-ion battery technologies [5].

Controlling CB yield, structure, morphology, and composition is essential for producing specific grades tailored to various applications in both conventional (e.g., furnace process [?]) and emerging production methods [6, 7, 8]. However, the influence of process parameters such as feedstock composition, pressure, and temperature-time history on CB properties remains incompletely understood due to the complexities of gas-phase chemistry and the intricate nature of CB formation (as discussed in the following sections). This highlights the need for robust computational models to predict yield, particle structure, and composition under different process conditions [9] and to mitigate soot emissions in combustion systems.

"soot" and "Carbon Black" are distinct materials in terms of chemical properties and synthesis process [10]. While soot usually refers to the unwanted particulate matter formed during incomplete combustion with variable organic content and a large variation in carbon to hydrogen (C/H) ratio [10], CB is commercially produced under highly controlled partial combustion or thermal decomposition of hydrocarbons. Soot particles generated under controlled laboratory condition has similar structure and composition to CB. The mature soot formed in methane and ethylene premixed flame can reach 95% elemental C/H ratio [11], which is close to CB composition. The comparison of transmission electron microscopy (TEM) images of industrially produced CB [12] with soot sampled from diesel fuel [13, 14] indicates similarity of their morphology and structure. Hereafter, soot will be used to collectively refer to carbonaceous nanoparticles produced in during combustion/pyrolysis processes.

Soot formation and evolution are believed to begin with the formation of Polycyclic Aromatic Hydrocarbons (PAHs) in the gas phase, followed by the transition of PAHs, which are widely accepted as major contributors to soot inception, into incipient particles—a process known as *soot inception*. This description of soot evolution is substantiated by experimental evidence. Transmission Electron Microscopy (TEM) analyses of soot sampled from flames [14], reactors [15], and engines [16] across various fuels and process conditions consistently reveal a fractal-like morphology, characterized by agglomerates of primary particles. The transition of PAHs into incipient soot, or soot inception, remains poorly understood at the level of pathways and elementary reactions [17]. This lack of understanding stems primarily from uncertainties in PAH chemistry and the kinetics of PAH growth into soot particles, a process that is highly reversible and thus sensitive to local conditions such as temperature, pressure, and the concentrations of intermediate species [17].

The classic description of soot inception relies on PAH dimerization where collision of two PAH molecules (monomers in this context) forms a dimer held together by Van der Wales forces [18]. The dimerization is an irreversible process with an efficiency that accounts for the reversibility or dissociation of dimers. The theory postulates that PAH growth continues by sequential addition of monomers forming stacks of dimers, trimers, tetramers and so on to reach a certain mass threshold that marks the emergence of incipient soot [18], but for practical purposes, a dimer is usually considered as incipient soot. Here, we call this model *Irreversible Dimerization*. Irreversible Dimerization has been used to predict soot formation in burner-stabilized premixed [19, 20], counterflow diffusion flames [21, 22], coflow diffusion flames [23, 24]. A collision efficiency factor ranging between 10^{-6} to 1 is also employed to adjust the inception flux and PAH adsorption rates to achieve desired soot mass and size distribution. PAHs of moderate sizes such as pyrene (4 rings) to coronene (7 rings) have been considered as the starting point of inception due to their thermodynamic instability that

2

justifies the irreversibility at high temperatures [18]. However, the theoretical calculations [25] and experiments [26] indicated that PAH dimerization is highly reversible in flame conditions. The inception flux of irreversible dimerization is mainly controlled by PAH concentration due to its weak temperature dependence, so it produces new particles at low temperatures (even less than 500 K) [27] despite experimental evidence for termination of inception below 1200 K [28, 29].

Kholghy et al. [30] emphasized on the necessity of chemical bond formation after physical PAH clustering for accurate prediction of volume fraction, primary particle diameter and PSD in ethylene coflow diffusion flames. Later, Kholghy et al. [31] proposed the *"Reactive Dimerization"* model which starts with reversible collision of PAHs leading to physical dimers held with vdW forces that are graphitized and form chemically-bonded dimers that serve as soot incipient particles that grow via coagulation and surface reactions. They also performed a systematic analysis on the contribution of different PAHs, and concluded that one- and two-ring aromatics account for almost all of inception flux in the so-called *"sooting flame"* [20]. However, Frenklach and Mebel [32] pointed out that an inception model that initiated with a highly reversible step similar to Reactive Dimerization [31] cannot produce sufficient flux of particles to match measurements of the benchmark burner-stabilized stagnation flame [33]. Instead, they proposed a Hydrogen-Abstraction/Carbon-Addition (HACA)-driven mechanism where addition of a monomer molecule to its radical activated by hydrogen abstraction forms a stable dimer via an E-Bridge bond formation, and this sequential process continues to form trimers, tetramers, and larger PAH clusters. Blanquart and Pitsch [34] proposed a two-step irreversible inception model were self collision of PAH with specified efficiencies results in formation of dimers that collide and subsequently coalesce into an incipient soot.

The gas-phase chemistry of aromatics can be extended to account for chemical growth of incipient soot via surface reactions [35]. This hypothesis, known as "chemical similarity" postulates that the reactions occurring on the soot surface are similar to those involving large molecules of PAHs in the gas phase. It also provides means to describe the rates of surface growth and particle oxidation in terms of elementary chemical reactions. In other words, it is assumed that the surface of soot particles is made up of lateral faces of larges PAHs covered with C-H bonds. This is the basis for HACA mechanism [18, 36] that assumes the soot surface to consist of hydrogenated sites with a predefined density. Mass growth on soot surface requires H-abstraction to form a radical site, followed by acetylene attack similar to growth of PAH molecules in the gas-phase. The reactivity of these sites changes with time and temperature [37, 38], described as soot aging. For modelling purposes, a temperature-dependent surface reactivity, usually represented by α, was introduced to account for these effects. Appel et al. [36] showed α changes with temperature and particle size.

Adsorption of PAHs on the surface of soot particles is also a viable growth mechanism [18], more specifically called physiorption or chemisorption depending on the mechanisms driving the adsorption process [39]. There is still debate over the stability of adsorbed PAH molecules on soot surface [40]. Following the hypothesis that PAHs are building blocks of soot particles, a mechanism similar to inception is often used to describe PAH-soot growth.

In typical soot formation processes, such as those occurring in flames and reactors, inception and surface growth are active for only a relatively short duration compared to the total residence time of soot particles. Subsequently, due to high particle concentrations, coagulation becomes the dominant mechanism, rapidly leading to the development of both a Self-Preserving Size Distribution (SPSD) [41] and an asymptotic fractal-like structure [42, 43]. The collision frequency of agglomerates depends on their evolving fractal-like morphology, with polydisperse agglomerates colliding more frequently than monodisperse ones. This enhancement reaches an asymptotic value of 35% [43] in the free molecular regime or 82% [44] in the transition regime at SPSD, irrespective of primary particle polydispersity.

Particle morphology, governed by inception, surface growth, and agglomeration, can be precisely tracked using mesoscale simulations such as Discrete Element Modeling (DEM) [45]. However, these methods are computationally expensive, and integrating them with chemical kinetics in Computational Fluid Dynamics (CFD) frameworks is challenging [46]. Consequently, their application is often limited to canonical scenarios where particle dynamics are solved independently of chemistry and flow dynamics—For instance, by populating the simulation domain with incipient particles—thereby bypassing the inception step—and neglecting gas removal or addition associated with soot forma-

tion [47] as it is difficult to have a particle dynamics modeled fully-coupled with gas chemistry.

As a computationally efficient alternative, particle dynamics can be tracked by Eulerian approaches such as the Method of Moments (MOM) [48] or Monodisperse Population Balance Models (MPBM) [49]. Such models only track average particle properties (e.g. moment ratios) and their accuracy could be limited if unrealistic assumptions (e.g. approximating agglomerates as monodisperse and perfect spheres) are used. However, when inception and surface growth are short [50] and high particle (number) concentrations are formed [47], they lead to rapid attainment of self-preserving size distributions (SPSD) and agglomerates having asymptotic structure [43]. In this case a MPBM or MOM can be assembled on a firm scientific basis with accuracy on par with DEM [45] and experimental data [51, 52, 53]. Such models can be readily interfaced with CFD simulations [54] without significant computational cost, making them ideal for three-dimensional and even turbulent flame simulations.

The MOM tracks moments of the PSD and estimates average particle properties such as mass [55], surface area [34], the number of constituent primary particles per agglomerate, n_p [48], or even particle composition [56] using the ratio of the moments. The MOM with interpolative closure (MOMIC) was developed to predict simultaneous nucleation, surface growth and coagulation of soot agglomerates and estimate its PSD with six equations [48]. To calculate source terms of the transported moments, additional moments that are not tracked are needed preventing the closure of the system of differential equations with the MOM [55, 57]. Thus, often the PSD shape is assumed a priori [55] or extra equations are solved to estimate it [49].In contrast, the MPBMs do not have the closure problem and calculate average particle properties by tracking their total concentration, mass [49] and area [58, 59].

Sectional Population Balance Models (SPBMs), similar to MPBMs but capable of tracking agglomerate and primary particle size distributions [60], are widely used in complex laminar [23] and turbulent flows [61]. Coupled with relations for fractal-like structure [62] and collision frequency [63], SPBMs accurately model particle size distribution, morphology, and composition. However, their computational cost rises exponentially with the number of sections [64] and tracked properties [23]. SPBMs are gaining attention, due to the recent increase in computational resources, for simulating laminar and turbulent benchmark flames in two-dimensional domains, even with moderately large chemical mechanisms. For example, the CoFlame solver [65], designed to simulate laminar diffusion flames in axisymmetric domains using SPBM, has been employed in numerous studies, demonstrating its ability to accurately capture PSD and other morphological properties [66, 67]. Kholghy et al. extended the SPBM in CoFlame to predict soot maturity by analyzing the equilibrium nanostructure of PAHs within soot primary particles, distinguishing nascent from mature soot based on an isotropic core-graphitic shell structure and surface PAH configuration [23]. More recent developments have further refined SPBMs by incorporating the persistent radical nature of soot particles, improving the description of nucleation, surface growth, and oxidation in laminar premixed and counterflow flames [68]. This approach employs a discrete-sectional method in which soot particles are tracked using discrete size bins (BINs), allowing detailed resolution of the size distribution and chemical composition. The algorithm systematically groups PAHs, primary particles, and aggregates into BINs based on carbon atom count and hydrogen-to-carbon ratio, capturing the evolution of particle size and morphology. By treating large PAHs and soot aggregates as resonantly stabilized radicals, the model reduces the reliance on explicit H-abstraction reactions and improves agreement with experimental data. However, the implementation relies on a customized chemical mechanism, which imposes constraints on modifying individual soot evolution processes, such as inception, growth, or oxidation, without adapting the entire framework [69, 70].

Here, we develop a computational package, called *omnisoot*, which integrates Cantera [71] as a chemistry solver to simulate soot formation in reduced-order dimensions. The package provides a versatile soot model that can be coupled with all reaction mechanisms. Two particle dynamics models—MPBM and SPBM—are incorporated, coupled with various soot inception and surface growth models, offering flexibility to study soot formation alongside gas-phase chemistry and predict its yield, morphology, composition, and size distribution. This package facilitates fundamental investigations of soot formation, including pathway analysis, reaction mechanism evaluation, and inception flux estimation, while also supporting process design and optimization of CB production

in industrial reactors under diverse fuel compositions, temperatures, pressures, and residence times. The theoretical background and governing equations for sub-models of omnisoot are detailed in subsequent sections, followed by validation against benchmark DEM simulations and verification of mass and energy conservation across all models. Finally, three use cases—shock tubes, flow reactors, and well-stirred reactors—demonstrate capability of omnisoot to predict gas chemistry, soot yield, structure, and size distribution.

2 Theoretical Foundation & Governing Equations

The mathematical basis for *omnisoot* is explained in the top-to-bottom hierarchical order. The reactors include the transport equations of gas mixture and "*soot variables*". The equation are different from pure gas phase transport formulation as they consider the solid phase. Soot model equations include a source term that represents how inception, surface growth, coagulation, and oxidation changes each tracked soot variable. The particle dynamics model describes size distribution and morphology of soot particles and calculates their collision rate, which is used to determine the coagulation source term. The *"PAH growth model"* take care of inception and adsorption from designated precursors and calculates the corresponding source terms. Similarly, the *"surface reactions"* model obtains the surface growth and oxidation rates based on HACA mechanism.

2.1 Assumptions and conventions

Here, the main conventions and assumptions used in the derivation of the mathematical model are listed below.

1. The ideal gas law is used to calculated physical, transport, and chemical properties of gas mixture.

2. $\dot{s}_k$ denotes the rate production/consumption of k_{th} gaseous species due to soot inception, surface growth and oxidation. It is positive when the species is released to gas mixture.

3. Each soot agglomerate consist of monodisperse spherical primary particles, which are in point contact. So, the model does not consider formation of necking in soot agglomerates by surface growth.

4. The word *"particle"* refers to soot both in spherical and agglomerate shape.

5. The density of soot is assumed constant at the value of 1800 kg/m^3. Soot density changes with its maturity level, which is often linked to the elemental C/H ratio of soot particles [72]. The considered value represents an average between density of mature soot with high C/H ratios ($\rho = 2000$kg/m^3) and that of nascent soot with low C/H ratios ($\rho = 1600$kg/m^3) [73, 72].

6. The incipient soot particles are 2 nm in diameter, so the model does not allow particles with a primary particle diameter smaller than 2 nm. The number of carbon atoms in the incipient soot particle ($n_{c,min}$) is calculated from the mass of a sphere with the diameter of 2 nm ($d_{p,min}$) assuming pure carbon content.

$$d_{p,min} = 2 \text{ nm}$$
$$n_{c,min} = \frac{\pi}{6}\rho_{soot}d_{p,min}^3\frac{1}{MW_c} \approx 378. \tag{1}$$

7. The calculation of PAH adsorption and soot oxidation requires "*soot concentration*" which is defined as the number of soot agglomerates per unit volume of gas. The number density of agglomerates, N_{agg}, are tracked per unit mass of gas mixture i.e. mol/kg_{gas}. So, soot concentration can be calculated by multiplying agglomerate number density by gas density as:

$$[\text{soot}] = \rho \cdot N_{agg}. \tag{2}$$

Table 1: The names, symbols, chemical formula and molecular weight of the soot precursors used by omnisoot

Species name	Symbol	Chemical formula	W [kg/mol]
Naphthalene	A2	$C_{10}H_8$	0.128
Phenanthrene	A3	$C_{14}H_{10}$	0.178
Pyrene	A4	$C_{16}H_{10}$	0.202
Acenaphthylene	A2R5	$C_{12}H_8$	0.152
Acephenanthrylene	A3R5	$C_{16}H_{10}$	0.202
Cyclopentapyrene	A4R5	$C_{18}H_{10}$	0.226

8. The specific heat, internal energy and enthalpy of soot are approximated by those of pure graphite, and employed to close the energy balance in the system [74].

9. Soot particles and gas are in thermal equilibrium during soot formation processes.

10. There is no temperature gradient within each agglomerate.

11. ψ denotes a *soot variable* that represents a mean property of soot particles (or a section) tracked in omnisoot by solving transport equations including total concentration of agglomerates, N_{agg} and primary particles, N_{pri}, and total carbon, C_{tot} and hydrogen content, H_{tot} of soot.

12. S_ψ is the source term of the soot variable, ψ that appears in soot equations. I_ψ represents the partial source terms i.e. the contribution of inception, PAH adsorption, surface growth, oxidation, and coagulation to each source term, S_ψ.

13. *PAH growth* is a sub-model of omnisoot with a set of pathways that determine the rate of inception and adsorption from PAHs (designated as soot precursors) in the gas mixture.

14. *Surface reactions* is a sub-model of omnisoot that describes the addition of acetylene to soot surface, and removal of carbon via oxidation by OH and O_2 following the HACA scheme. The model does not consider soot oxidation with CO_2, H_2O and NO_x.

15. The single superscript, i denotes the section number of a soot variable or a derived property. For example, d_p^i is the primary particle diameter of section i. The double superscript, ij represents a property related to two sections. For example, β^{ij} is the collision frequency of the sections i and j. In case of the monodisperse model, the section number can be ignored because it is equivalent to the sectional model with one section.

16. The computation of morphological parameters (d_p, d_m, d_g, and n_p) and diffusion coefficient are done similarly in both particle dynamics models, but they are explained separately in standalone sections.

17. *precursors* refers to the PAHs larger than naphthalene used for inception and surface growth (PAH adsorption). The list of precursors with their chemical formula and molecular mass is provided in Table 1. It should be noted that the precursors can be dynamically changed by omnisoot's user interface.

2.2 Constant Volume Reactor (CVR)

This reactor assumes that the volume of system does not change during the process. In the absence of soot, this leads to a gas mixture with constant density. However, soot formation converts part of gaseous species to solid particles thereby affecting its volume and density. Note that, continuity, species and energy transport equations only track gas mixture properties. Figure 1 illustrates the

control volume around the gas mixture targeted by mass and energy balance equations. Any mass converted to solid soot particles leaves the control volume. Mass and energy passes through the control surface around solid particles by soot formation processes. The volume of gas mixture changes during the process but the reactor volume (the sum of volume of gas mixture and solid particles) stays constant.
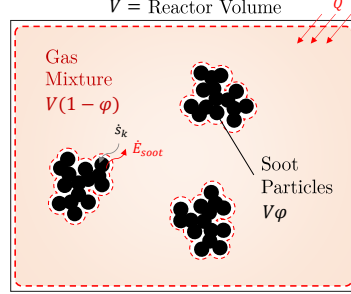

Figure 1: The schematics of control volume considered for the constant volume reactor that encompasses the gas mixture and excludes the soot particles. Mass and energy are transferred between gas and soot particles.

The rate of change of gas mass is described as:

$$\frac{d}{dt}(m) = (1 - \varphi) \sum_i \dot{s}_i W_i. \tag{3}$$

Similarly, the species equation for species k is expressed as:

$$\frac{dY_k}{dt} = \frac{1}{\rho} \left(\dot{\omega}_k + \dot{s}_k \right) W_k - \frac{1}{\rho} Y_k \sum_i \dot{s}_i W_i. \tag{4}$$

The transport equation for a generic soot variable, ψ can be written as:

$$\frac{d\psi}{dt} = S_\psi - \frac{\psi}{\rho} \sum_i \dot{s}_i W_i. \tag{5}$$

The energy balance for the gas mixture is simplified to the rate change of temperature. An external heat source of $\dot{Q}$ is considered to account for possible heat loss/gain of the reactor.

$$\frac{dT}{dt} = \frac{1}{\rho(1-\varphi)c_v + \rho_{soot}\varphi c_{soot}} \left[-(1-\varphi) \sum_k e_k \left(\dot{\omega}_k + \dot{s}_k \right) W_k \right.$$
$$\left. + u_{soot}(1-\varphi) \sum_k \dot{s}_k W_k + \frac{\dot{Q}}{V} \right]. \tag{6}$$

2.3 Constant Pressure Reactor (CPR)

This reactor is a closed system similar to CVR, but the pressure stays constant throughout the process and the boundaries of the system can move and change its volume. Figure 2 shows an illustration of constant pressure reactor. Similarly, the heat transfer can occur through reactor walls and soot particles, which changes the internal energy of gas mixture.

The rate change of mass, species, and soot variables for the constant pressure reactor (CPR) are the same as CVR given in Equations 3, 4, and 5, respectively. The energy equation is written as:
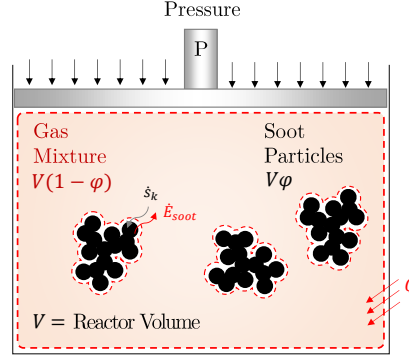
Figure 2: The schematics of control volume in the pressure reactor around the gas mixture excluding the soot particles. Mass and energy pass through the boundaries of gas and soot.

$$\frac{dT}{dt} = \frac{1}{\rho(1-\varphi)c_p + \rho_{soot}\varphi c_{soot}} \left[-(1-\varphi)\sum_k h_k \left(\dot{\omega}_k + \dot{s}_k \right) W_k \right. \tag{7}$$
$$\left. +h_{soot}(1-\varphi)\sum_k \dot{s}_k W_k + \frac{\dot{Q}}{V} \right].$$

2.4 Perfectly Stirred Reactor

In this reactor, gas enters with a mass flow rate $\dot{m}_{in}$, composition of Y_{in} and temperature of T_{in}, instantaneously mixes and homogeneously reacts with the mixture resident inside the reactor. The reacting gas reaches a spatially uniform temperature and composition described by T, and Y. It is assumed that temperature, composition and soot properties of the outflow are the same as reactor. Figure 3 illustrates the schematics of PSR. $\dot{m}_{in}$ and $\dot{m}_{out}$ refer to inflow and outflow gas mass flow rates, respectively. Under no-soot conditions, the inlet and outlet mass flow rates are equal, but the gas mixture loses mass by soot formation, so $\dot{m}_{out}$ is slightly less than $\dot{m}_{in}$. The pressure of reactor is assumed to stay constant during the process [75]. The nominal residence time of gas mixture in the reactor is defined as:

$$\tau = \frac{\rho V}{\dot{m}_{in}}. \tag{8}$$

The conservation of mass can be written for PSR by considering the mass flux of in- and outflow, and the removal of mass due to soot generation as:

$$\frac{dm}{dt} = \dot{m}_{in} - \dot{m}_{out} + (1-\varphi)\sum_i \dot{s}_i W_i. \tag{9}$$

The density is not determined by solving the continuity equation, but rather from ideal gas law and assuming a constant pressure and the composition from solving the species transport equations as:

$$\frac{dY_k}{dt} = \frac{1}{\tau}\left(Y_{k,in} - Y_k\right) + \frac{1}{\rho}\left[\left(\dot{\omega}_k + \dot{s}_k \right) W_k - Y_k \sum_i \dot{s}_i W_i \right]. \tag{10}$$

The soot transport equations can also be expressed as:

$$\frac{d\psi}{dt} = \frac{\dot{m}_{in}}{\rho V (1-\varphi)}\left(\psi_{in} - \psi\right) + S_\psi - \frac{1}{\rho}\psi\sum_i \dot{s}_i W_i. \tag{11}$$
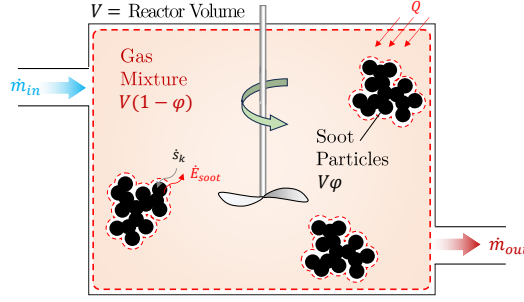
8

Figure 3: The schematics of control volume considered for the perfectly stirred reactor that encompasses the gas mixture and excludes the soot particles. Mass and energy are transferred between gas and soot particles. The inlet flow brings species and enthalpy into the control volume and the outlow discharges them. The gas mass flow at the outlet is less inlet due to partial conversion of gaseous species to soot.

The energy equation for this reactor is written as:

$$
\frac{dT}{dt} = \frac{1}{\rho\left(1-\varphi\right)c_p + \rho_{soot}c_{p,soot}\varphi}\left[\frac{\dot{m}_{in}}{V}\left(h_{in} - h\right) - \frac{\dot{m}_{in}}{V}\sum_k\left(Y_{k,in} - Y_k\right)h_k\right.
$$
$$
\left. - \left(1-\varphi\right)\sum_k\left(\dot{\omega}_k + \dot{s}_k\right)W_k h_k + \left(1-\varphi\right)\sum_i \dot{s}_i W_i h_{soot} + \frac{\dot{Q}}{V}\right]. \tag{12}
$$

2.5   Plug Flow Reactor

The plug flow reactor (PFR) is an ideal representation of a channel or duct with a steady-state one-dimensional flow changes temperature, composition, and soot properties along the channel. The There is no spatial gradient over the cross-section due to strong mixing. Diffusion along the channel is negligible. The pressure is assumed constant along the reactor.
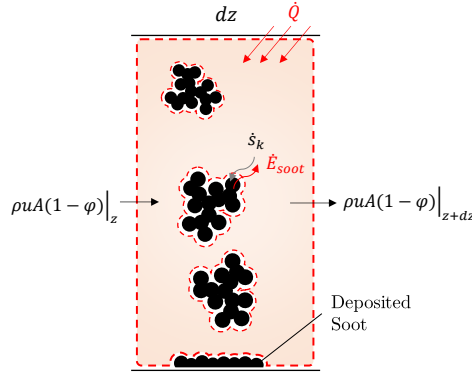

Figure 4: The schematics of control volume for a differential element along PFR that includes the gas mixture and excludes the soot particles considering wall heat transfer. The model considers mass and energy are transfer between gas and soot as well as wall deposition along the reactor.

The continuity equation for PFR is written as:

$$
\frac{d\dot{m}}{dz} = (1-\varphi)A\sum_i \dot{s}_i W_i. \tag{13}
$$

9

The momentum equation can also be established as:

$$u(1 - \varphi) \sum_i \dot{s}_i W_i + \rho u(1 - \varphi)\frac{du}{dz} = -\frac{d}{dz}(p(1 - \varphi)) - \frac{\tau_w}{R_H}. \tag{14}$$

where τ_w is the wall shear the can be determined from fraction factor, f as:

$$\tau_w = \frac{1}{2}\rho u^2 f. \tag{15}$$

The friction factor, f can be calculated with a good accuracy for the entire range of Reynolds number, Re, from laminar to turbulent flow using the explicit formula given by Haaland [76]:

$$\frac{1}{f^{1/2}} = -1.8\log\left(\frac{6.9}{Re} + \left[\frac{\epsilon/D_H}{3.7}\right]^{1.11}\right), \tag{16}$$

where ϵ is the roughness of reactor wall. R_H and D_H are hydraulic radius and diameter, respectively that can be determined from cross-section geometry of reactor as:

$$D_H = 4R_H = \frac{4A_c}{P_c}, \tag{17}$$

where A_c and P_c are cross-sectional area and wetted perimeter of the reactor. The species equation can be expressed as:

$$\frac{dY_k}{dz} = \frac{1}{\rho u}\left[(\dot{\omega}_k + \dot{s}_k)W_k - Y_k\sum_i \dot{s}_i W_i\right]. \tag{18}$$

The soot transport equations can also be written as:

$$\frac{d\psi}{dz} = \frac{S_\psi}{u} - \frac{\psi}{\rho u}\sum_i \dot{s}_i W_i - \frac{4}{D_H}\frac{k_{dep}^i \psi}{u}. \tag{19}$$

where k_{dep}^i is the deposition velocity of soot particles of section i calculated as:

$$k_{dep} = \frac{Sh \cdot D^i}{D_H}. \tag{20}$$

where Sh is the Sherwood number, which is 3.66 for a laminar flow and calculated using the Berger and Hau correlation [77] for the turbulent flow in terms of Re and Sc, Schmidt number as:

$$Sh = 0.0165Re^{0.86}Sc^{1/3}. \tag{21}$$

The energy equation can be expressed as:

$$\frac{dT}{dz} = \frac{1}{\rho u(1 - \varphi)c_p + \rho_{soot}u\varphi c_{p,soot}}\left[-(1 - \varphi)\sum_k h_k(\dot{\omega}_k + \dot{s}_k)W_k \right.$$
$$\left. +h_{soot}(1 - \varphi)\sum_k \dot{s}_k W_k + q''\frac{P_c}{A}\right]. \tag{22}$$

where q'' is the wall heat flux provided as a function of reactor length or flow residence time that represents external heating or heat loss in the reactor.

2.6 Particle Dynamics

Population balance models rely on the Eulerian description of particles where bulk properties of particle population such as number density, mass or surface area are treated as continuous quantities and tracked by solving scalar transport equations. These methods are computationally cheaper compared with mesoscale models such as DEM, and can be easily interfaced with chemical kinetics in CFD solvers to simulate soot formation in turbulent configurations. Here, we use two particle dynamics models: a monodisperse population balance model (MPBM) based on four variables leading to 4 transport equations in total, and a fixed sectional population balance model (SPBM) tracking three variables per section. The total number of transport equations in the sectional model is determined by the number of sections and number of equations solved per section. The first two/three variables in the MPBM/SPBM enables description of number, mass, and evolving fractal-like morphology of soot agglomerates that are necessary to accurately predict collision frequency of agglomerates [78] as well as oxidation and surface growth rates [79]. The last variable tracks the number of hydrogen atoms in agglomerates that allows the model to capture the soot composition, thereby its maturity [23], and surface reactivity [56]. The tracked variables are used to address particle dynamics that includes (i) reconstructing particles morphology by determining characteristic diameters from tracked soot variables, (ii) calculating collision frequency and coagulation source term, (iii) combining the contribution of inception, PAH adsorption, surface growth and oxidation into source terms. First, common features of both particle dynamics models are reviewed. As mentioned before, any parameter with superscript i denotes the section number, which can be ignored/dropped for the MPBM that only has one section. For example, d_m^i can be replaced with d_m.

2.7 Soot Morphology

The evolving fractal-like structure of agglomerates is quantified by their mobility diameter normalized by primary particle, d_m/d_p, and gyration, d_m/d_g, diameters that can be described with power-laws derived from mesoscale simulations. Incipient soot is initially a sphere formed of PAHs with constant density that grows in size by surface reactions and forms agglomerates by coagulation. The collision frequency of particles depends on their evolving fractal-like structure [78]. Some simplifying assumptions are made to reconstruct the particle morphology from tracked variables. The primary particles of each agglomerate are similar enough that can be described by mean size and composition. They also stay in point contact during surface growth and agglomeration i.e. the necking is ignored. Mobility and gyration diameters are calculated using power-laws developed to describe the morphology of soot from premixed [51], diffusion [80] flames, and diesel engines [81]. Figure 5 illustrates the schematics of a soot agglomerates with 12 primary particles and depicted d_p, d_m, and d_g.

n_p^i is the number of primary particles per agglomerate of ith section that can be obtained by dividing the number concentration of primary particles in i^{th} section by that of agglomerates in that section as:

$$n_p^i = \frac{N_{pri}^i}{N_{agg}^i}. \tag{23}$$

Primary particle diameter, d_p^i, can be obtained from total carbon content and number density of primary particles using

$$d_p^i = \left(\frac{6}{\pi} \frac{C_{tot}^i \cdot W_{carbon}}{\rho_{soot}} \frac{1}{N_{pri}^i \cdot Av} \right)^{1/3}. \tag{24}$$

The DEM-derived power-laws [47] relate d_m^i and d_g^i to d_p^i and n_p^i as

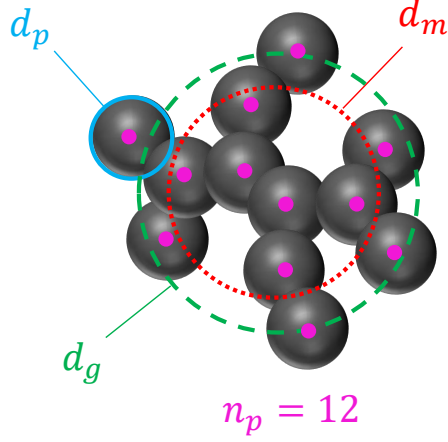$$d_m^i = d_p^i \cdot n_p^{i\,0.45}, \tag{25}$$

11

Figure 5: The schematics of a soot agglomerates with 12 primary particles ($n_p = 12$). Primary particle (d_p), mobility (d_m), and gyration (d_g) are shown.

$$d_g^i = \begin{cases} d_m^i/(n_p^{i\,-0.2} + 0.4), & \text{if } n_p^i > 1.5 \\ d_m^i/1.29. & \text{if } n_p^i \leq 1.5 \end{cases} \tag{26}$$

The collision diameter, d_c^i is the maximum of d_m^i, d_g^i:

$$d_c^i = \max\left(d_m^i, d_g^i\right) \tag{27}$$

d_m^i, d_g^i, d_c^i are used to calculate the source terms of the surface growth, oxidation, PAH adsorption and coagulation. The volume equivalent diameter, d_v^i, is the diameter of the sphere with the same mass as agglomerate, and it is obtained as:

$$d_v^i = d_p^i \cdot n_p^{i\,1/3}. \tag{28}$$

The primary particle surface area is calculated from d_p^i assuming spherical primary particles.

$$A_p^i = \pi d_p^{i\,2}, \tag{29}$$

A_{tot}^i (for each section) is defined as the total surface area of soot particles per unit mass of gas mixture obtained as

$$A_{tot}^i = N_{pri}^i \cdot Av \cdot A_p^i. \tag{30}$$

2.8 Diffusion of soot particles

The diffusion coefficient of soot particle, D^i, is calculated as

$$D^i = \frac{k_B T}{f^i}, \tag{31}$$

where f^i is the friction factor of particles in gas,

$$f^i = \frac{3\pi\mu d_m^i}{C^i(d_m^i)}, \tag{32}$$

where C^i is the Cunningham function, which applies a correction to the particle friction factor in the continuum regime to account for non-continuum effects in the transition and free molecular regimes, as:

$$C^i(d) = 1 + \frac{2\lambda}{d}\left(1.21 + 0.4 \cdot \exp(\frac{-0.78d}{\lambda})\right), \tag{33}$$

where λ is the mean free path of gas given as:

$$\lambda = \frac{\mu}{\rho}\sqrt{\frac{\pi W_{gas}}{2k_B AvT}}. \tag{34}$$

Note that, λ is a property of the gas mixture that does not depend on particle morphology and size section. The mean velocity, c^i and mean stop distance of particles, λ_a^i can be calculated as:

$$c^i = \sqrt{\frac{8k_B T}{\pi m_{agg}^i}}. \tag{35}$$

$$\lambda_a = \frac{8D^i}{\pi c^i}. \tag{36}$$

The mean distance of particles is also calculated as:

$$\delta_a^i = \frac{1}{d_c^i \lambda_a^i}\left[\left(d_c^i + \lambda_a^i\right)^3 - \left(d_c^{i\,2} + \lambda_a^{i\,2}\right)^{3/2}\right] - d_{c,j}. \tag{37}$$

2.9   Coagulation efficiency of soot particles

The coagulation efficiency of soot particles is commonly assumed as unity meaning that every collision between two soot particles successfully results in formation of a new agglomerate. However, numerical models [82] and experimental evidence [83] showed that the coagulation efficiency drastically decrease for particles smaller than 10 nm in the free molecular regime (Kn>>10) due to their high kinetic energy that exceeds the attractive forces [84]. The coagulation efficiency of two colliding particles can be described as [82]:

$$\zeta^{ij} = 1 - \left(1 + \frac{\Phi_0^{ij}}{k_B T}\right)\exp\left(-\frac{\Phi_0^{ij}}{k_B T}\right), \tag{38}$$

where Φ_0 is the potential well depth i.e. the minimum interaction energy between two colliding particles. Hou et al. [85] calculated Φ_0 for soot particles 1-15 nm by considering the attraction and repulsion between constituent carbon and hydrogen atoms, and proposed a equation based on the reduced diameter, d_r^{jk} of colliding particles as:

$$\Phi_0^{ij} = -6.6891 \times 10^{-23}(d_r^{jk})^3 + 1.244 \times 10^{-21}(d_r^{jk})^2 + 1.1394 \times 10^{-20}d_r^{jk} - 5.5373 \times 10^{-21} \tag{39}$$

$$d_r^{jk} = \frac{d_c^i \cdot d_c^j}{d_c^i + d_c^j} \tag{40}$$

Equation (39) is valid for d_r^{jk} between 1 and 7 nm, and ζ^{ij} is assumed as 1 for particles with reduced diameter larger than 7 nm.

2.10   Soot Composition

The composition of soot is characterized by their elemental carbon to hydrogen ratio (C/H) is a measure of soot maturity and increases from C/H < 2 for incipient soot [86] to 2 < C/H < 10 for nascent soot [87] and C/H > 20 for mature soot [88]. The soot agglomerates are assumed to have pure carbon graphitic core [23] with all hydrogen atoms on the surface [56]. C/H ratio can be obtained from total carbon and hydrogen content as:

$$\left(\frac{C}{H}\right)^i = \frac{C_{tot}^i}{H_{tot}^i}. \tag{41}$$

The carbon content of each agglomerate is a predefined parameter in the SPBM (depending on the section the agglomerate is placed), but it can be calculated from dividing C_{tot} by N_{agg} for the MPBM. The hydrogen content of each agglomerate is calculated for both particle dynamics models as:

$$H_{agg}^i = \frac{H_{tot}^i}{N_{agg}^i}. \tag{42}$$

2.11 Monodisperse Population Balance Model

The MPBM used in this research tracks the number density of primary particles (N_{pri}) and agglomerates (N_{agg}), total carbon (C_{tot}) and hydrogen (H_{tot}) content of soot particles per unit mass of gas mixture. The morphological parameters such as primary particle, mobility and gyration diameters obtained from these soot variables are the average values for the population.

2.11.1 Coagulation

Coagulation is the process during which solid and hard soot particles collide and attach at point of contact leading to larger agglomerates. This process conserves the soot mass and composition and number density of primary particles, so coagulation only affects N_{agg}. I_{coag} accounts for the decay rate of N_{agg} by the binary collision of soot particles by

$$I_{coag} = -\frac{1}{2}\zeta\beta N_{agg}^2, \tag{43}$$

where β is the collision frequency of agglomerates for the free molecular (Kn > 10) to continuum regime (Kn < 0.1), and ζ is the coagulation efficiency calculated by Equation 38. The value of β in the transition regime (0.1 < Kn < 10) can be calculated from the harmonic mean of the continuum (β_{cont}) and free molecular (β_{fm}) regime values. Additionally, an enhancement factor of %82 is applied to take into account the effect of polydispersity [44] in the monodisperse as:

$$\beta = 1.82\frac{\beta_{fm}\beta_{cont}}{\beta_{fm} + \beta_{cont}}, \tag{44}$$

$$\beta_{fm} = 4\sqrt{\frac{\pi k_b T}{m_{agg}}}d_c^2, \tag{45}$$

$$\beta_{cont} = 8\pi d_c D. \tag{46}$$

Alternatively, β can be obtained using Fuchs interpolation [89] as:

$$\beta = \beta_{cont}\left(\frac{d_c}{d_c + 2\sqrt{2}\delta} + \frac{8D}{\sqrt{2}c_r d_c}\right)^{-1}. \tag{47}$$

2.11.2 Source terms

The source terms of tracked variables combines the effect of the inception, PAH adsorption, surface growth and oxidation and coagulation.

$$S_{N_{agg}} = \frac{I_{N,inc}}{n_{c,min}} + I_{coag}. \tag{48}$$

$$S_{N_{pri}} = \frac{I_{N,inc}}{n_{c,min}}. \tag{49}$$

$$S_{C_{tot}} = I_{C_{tot},inc} + I_{C_{tot},gr} + I_{C_{tot},ads} + I_{C_{tot},ox}. \tag{50}$$

$$S_{H_{tot}} = I_{H_{tot},inc} + I_{H_{tot},gr} + I_{H_{tot},ads} + I_{H_{tot},ox}. \tag{51}$$

The partial source terms in Equations 48-51 denoted by I are determined by PAH growth and surface reaction model explained in Sections 2.14 and 2.13, respectively.

2.12 Sectional Population Balance Model

A SPBM with the fixed pivot is used to describe particle dynamics [90]. The mass range of particles are divided into discrete sections each of which includes agglomerates of the same mass. Inception introduces new particles to the first section with the mass corresponding to the incipient particle (≈ 378 carbon atoms). The particles of first section can migrate to upper sections by gaining mass via surface growth and coagulation, and return to lower sections when they lose mass through oxidation. Particle fragmentation is not considered. The mass of sections is determined by a geometric progression with a scale factor equal to the mass of incipient soot particle, and a common ratio of SF, known as sectional spacing factor, defaulted to 60 and 1.5, respectively, but both parameters can be dynamically changed from the user interface of omnisoot. The mass of each section is approximated by the carbon content of agglomerates in moles as:

$$C_{agg}^i = \frac{n_{c,min}}{Av} \cdot SF^{(i-1)}. \tag{52}$$

where (i-1) represents the exponent of SF. The mass of hydrogen is ignored in the placement of agglomerates in the sections. The total number density of agglomerates, N_{agg}^i[mol/kg], and primary particles, N_{pri}^i[mol/kg] are tracked for each section. Morphological parameters are determined for each section according to the equations in Section 2.7.
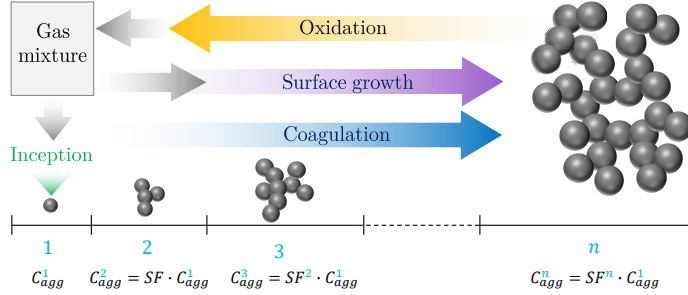

Figure 6: The illustration of sections of SPBM. The mass of sections grows progressively by the scale factor of SF. Inception introduces new particles to the first section that propagate to the upper section via coagulation and surface growth and return to lower sections by oxidation.

2.12.1 Coagulation

In SPBM approach, collisions between particles from every two sections are considered. The new particles formed by coagulation are placed in an upper section with the mass equal to sum of mass of particles involved in the collision. When the mass of yielded particle lies between two consecutive sections, the particles are divided among these sections proportional to their mass. One possible scenario is that the mass of the newly formed particle is greater than the last section, thus leaving tracked mass range. Losing mass is a potential problem with the fixed pivot sectional model, which can be avoided by selecting proper number of sections and spacing factor to keep the number of agglomerates to a minimum in the last sections during the simulation.

The collision frequency between sections j and k can be obtained from the harmonic mean of the values in the continuum and free molecular regimes as:

$$\beta^{jk} = \frac{\beta_{fm}^{jk} \beta_{cont}^{jk}}{\beta_{fm}^{jk} + \beta_{cont}^{jk}}, \tag{53}$$

$$\beta_{fm}^{jk} = \sqrt{\frac{\pi k_b T}{2} \left(\frac{1}{m_{agg}^j} + \frac{1}{m_{agg}^k} \right)} \left(d_c^j + d_c^k \right)^2, \tag{54}$$

15

$$\beta_{cont}^{ij} = \frac{2k_B T}{3\mu} \left(\frac{C^j}{d_m^j} + \frac{C^k}{d_m^k} \right) \left(d_c^j + d_c^k \right)^2. \tag{55}$$

The collision frequency can also be determined from the Fuchs interpolation similar to the MPBM as:

$$\beta^{jk} = \beta_{cont}^{ij} \left[\frac{d_c^j + d_c^k}{d_c^j + d_c^k + 2 + \delta_r^{jk}} + \frac{8 \left(D^j + D^k \right)}{\bar{c}_r^{jk} \left(d_c^j + d_c^k \right)} \right]^{-1}, \tag{56}$$

where δ_r^{jk} and $\bar{c}_r^{jk}$ are the mean square root of mean distance and velocity of particles, respectively.

$$\delta_r^{jk} = \sqrt{\delta_a^{j\,2} + \delta_a^{k\,2}}, \tag{57}$$

$$\bar{c}_r^{jk} = \sqrt{c^{j\,2} + c^{k\,2}}. \tag{58}$$

Coagulation redistributes the total number of agglomerates and primary particles as well as hydrogen atoms among the sections. The partial coagulation source terms for N_{agg}^i, N_{pri}^i and H_{tot}^i can be calculated as:

$$I_{N_{agg}}^i = \sum_{k=1}^{n_{sec}} \sum_{j=k}^{n_{sec}} \left(1 - \frac{\delta_{jk}}{2} \right) \eta_{ijk} \zeta^{jk} \beta^{jk} N_{agg}^j N_{agg}^k - N_{agg}^i \sum_{k=1}^{n_{sec}} \zeta^{im} \beta^{im} N_{agg}^m. \tag{59}$$

$$I_{N_{pri}}^i = \sum_{k=1}^{n_{sec}} \sum_{j=k}^{n_{sec}} \left(1 - \frac{\delta_{jk}}{2} \right) \eta_{p,ijk} \eta_{ijk} \zeta^{jk} \beta^{jk} N_{agg}^j N_{agg}^k - N_{pri}^i \sum_{k=1}^{n_{sec}} \zeta^{im} \beta^{im} N_{agg}^m. \tag{60}$$

$$I_{H_{tot}}^i = \sum_{k=1}^{n_{sec}} \sum_{j=k}^{n_{sec}} \left(1 - \frac{\delta_{jk}}{2} \right) \eta_{h,ijk} \eta_{ijk} \zeta^{jk} \beta^{jk} N_{agg}^j N_{agg}^k - H_{tot}^i \sum_{k=1}^{n_{sec}} \zeta^{im} \beta^{im} N_{agg}^m. \tag{61}$$

where δ_{jk} is the Kronecker delta defined as:

$$\delta_{jk} = \begin{cases} 1, & \text{if } j = k \\ 0. & \text{if } j \neq k \end{cases} \tag{62}$$

In Equation (59), η_{ijk} assigns newly formed agglomerates to the two consecutive section in order to conserves mass during coagulation [91].

$$\eta_{ijk} = \begin{cases} \dfrac{C_{agg}^{i+1} - C_{agg}^{jk}}{C_{agg}^{i+1} + C_{agg}^i}, & \text{if } C_{agg}^i \leq C_{agg}^{jk} < C_{agg}^{i+1} \\[3mm] \dfrac{C_{agg}^i - C_{agg}^{jk}}{C_{agg}^i + C_{agg}^{i-1}}, & \text{if } C_{agg}^{i-1} \leq C_{agg}^{jk} < C_{agg}^i \\[3mm] 0 & \text{else} \end{cases} \tag{63}$$

where $C_{agg}^{jk} = C_{agg}^j + C_{agg}^k$. Similarly, $\eta_{p,ijk}$ in Equation (60) and $\eta_{h,ijk}$ in Equation (61) adjust the number primary particles and hydrogen atoms added to consecutive sections based on their mass, respectively.

$$\eta_{p,ijk} = \frac{C_{agg}^i}{C_{agg}^{jk}} \left(n_p^j + n_p^k \right), \tag{64}$$

$$\eta_{h,ijk} = \frac{C_{agg}^i}{C_{agg}^{jk}} \left(H_{agg}^j + H_{agg}^k \right), \tag{65}$$

2.12.2 Source terms

The source terms are split into four parts showing the contribution of different soot formation and evolution factors. The effect of surface growth and PAH adsorption are combined (denoted by the subscript gr,ads) because they are similar mass-gaining mechanisms.

$$S_{N_{agg}} = \left(S_{N_{agg}}\right)_{inc} + \left(S_{N_{agg}}\right)_{gr,ads} + \left(S_{N_{agg}}\right)_{ox} + \left(S_{N_{agg}}\right)_{coag}, \tag{66}$$

$$S_{N_{pri}} = \left(S_{N_{pri}}\right)_{inc} + \left(S_{N_{pri}}\right)_{gr,ads} + \left(S_{N_{pri}}\right)_{ox} + \left(S_{N_{pri}}\right)_{coag}, \tag{67}$$

$$S_{H_{tot}} = \left(S_{H_{tot}}\right)_{inc} + \left(S_{H_{tot}}\right)_{gr,ads} + \left(S_{H_{tot}}\right)_{ox} + \left(S_{H_{tot}}\right)_{coag}. \tag{68}$$

Inception introduces equal number of agglomerates and primary particles to the first section.

$$\left(S_{N_{agg}}\right)_{inc} = \frac{1}{Av}\frac{I_{N,inc}}{C_{agg}^i}, \quad i = 1. \tag{69}$$

$$\left(S_{N_{pri}}\right)_{inc} = \frac{1}{Av}\frac{I_{N,inc}}{C_{agg}^i}, \quad i = 1. \tag{70}$$

$$\left(S_{H_{tot}}\right)_{inc} = I_{H,inc}, \quad i = 1. \tag{71}$$

Surface growth and PAH adsorption increase the carbon and hydrogen content of agglomerates, and transfer them to upper sections. The removal rate of agglomerates (N_{agg}^i) from the original section due to surface growth and PAH adsorption must be equal to the addition rate of agglomerates to the target section to conserve the mass, and it is calculated by dividing the mass growth rate by the difference of the mass of the adjacent sections.

$$\left(S_{N_{agg}}\right)_{gr,ads} = \frac{1}{Av}\begin{cases} -\dfrac{I_{C_{tot},gr}^i + I_{C_{tot},ads}^i}{C_{agg}^{i+1} - C_{agg}^i} & \text{if } i = 1 \\[3mm] \dfrac{I_{C_{tot},gr}^{i-1} + I_{C_{tot},ads}^{i-1}}{C_{agg}^i - C_{agg}^{i-1}} - \dfrac{I_{C_{tot},gr}^i + I_{C_{tot},ads}^i}{C_{agg}^{i+1} - C_{agg}^i} & \text{if } 1 < i < n_{sec} \\[3mm] \dfrac{I_{C_{tot},gr}^{i-1} + I_{C_{tot},ads}^{i-1}}{C_{agg}^i - C_{agg}^{i-1}} & \text{if } i = n_{sec} \end{cases} \tag{72}$$

As agglomerates move up/down through sections, they carry the number of primary particles as well as hydrogen atoms, so the transfer rate of agglomerates is multiplied by n_p^i and H_{agg}^i, respectively.

$$\left(S_{N_{pri}}\right)_{gr,ads} = \frac{1}{Av}\begin{cases} -\dfrac{I_{C_{tot},gr}^i + I_{C_{tot},ads}^i}{C_{agg}^{i+1} - C_{agg}^i} & \text{if } i = 1 \\[3mm] \dfrac{I_{C_{tot},gr}^{i-1} + I_{C_{tot},ads}^{i-1}}{C_{agg}^i - C_{agg}^{i-1}} n_p^{i-1} - \dfrac{I_{C_{tot},gr}^i + I_{C_{tot},ads}^i}{C_{agg}^{i+1} - C_{agg}^i} n_p^i & \text{if } 1 < i < n_{sec} \\[3mm] \dfrac{I_{C_{tot},gr}^{i-1} + I_{C_{tot},ads}^{i-1}}{C_{agg}^i - C_{agg}^{i-1}} n_p^{i-1} & \text{if } i = n_{sec} \end{cases} \tag{73}$$

$$(S_{H_{tot}})_{gr,ads} = \frac{1}{Av} \begin{cases} -\dfrac{I_{C_{tot},gr}^i + I_{C_{tot},ads}^i}{C_{agg}^{i+1} - C_{agg}^i} H_{agg}^i + I_{H_{tot},gr}^i + I_{H_{tot},ads}^i & \text{if } i = 1 \\[3ex] \dfrac{I_{C_{tot},gr}^{i-1} + I_{C_{tot},ads}^{i-1}}{C_{agg}^i - C_{agg}^{i-1}} H_{agg}^{i-1} - \dfrac{I_{C_{tot},gr}^i + I_{C_{tot},ads}^i}{C_{agg}^{i+1} - C_{agg}^i} H_{agg}^i + I_{H_{tot},gr}^i + I_{H_{tot},ads}^i & \text{if } 1 < i < n_{sec} \\[3ex] \dfrac{I_{C_{tot},gr}^{i-1} + I_{C_{tot},ads}^{i-1}}{C_{agg}^i - C_{agg}^{i-1}} H_{agg}^{i-1} + I_{H_{tot},gr}^i + I_{H_{tot},ads}^i & \text{if } i = n_{sec} \end{cases}$$

$$(74)$$

Similarly, the agglomerates lose (carbon) mass by oxidation, and descend to the lower sections carrying primary particle and hydrogen.

$$\left(S_{N_{agg}}\right)_{ox} = \frac{1}{Av} \begin{cases} \dfrac{I_{C_{tot},ox}^{i+1}}{C_{agg}^{i+1} - C_{agg}^i} - \dfrac{I_{C_{tot},ox}^i}{C_{agg}^i} & \text{if } i = 1 \\[3ex] \dfrac{I_{C_{tot},ox}^{i+1}}{C_{agg}^{i+1} - C_{agg}^i} - \dfrac{I_{C_{tot},ox}^i}{C_{agg}^i - C_{agg}^{i-1}} & \text{if } 1 < i < n_{sec} \\[3ex] -\dfrac{I_{C_{tot},ox}^i}{C_{agg}^i - C_{agg}^{i-1}} & \text{if } i = n_{sec} \end{cases}$$

$$(75)$$

$$\left(S_{N_{pri}}\right)_{ox} = \frac{1}{Av} \begin{cases} \dfrac{I_{C_{tot},ox}^{i+1}}{C_{agg}^{i+1} - C_{agg}^i} n_p^{i+1} - \dfrac{I_{C_{tot},ox}^i}{C_{agg}^i} & \text{if } i = 1 \\[3ex] \dfrac{I_{C_{tot},ox}^{i+1}}{C_{agg}^{i+1} - C_{agg}^i} n_p^{i+1} - \dfrac{I_{C_{tot},ox}^i}{C_{agg}^i - C_{agg}^{i-1}} n_p^i & \text{if } 1 < i < n_{sec} \\[3ex] -\dfrac{I_{C_{tot},ox}^i}{C_{agg}^i - C_{agg}^{i-1}} n_p^i & \text{if } i = n_{sec} \end{cases}$$

$$(76)$$

$$(S_{H_{tot}})_{ox} = \frac{1}{Av} \begin{cases} \dfrac{I_{C_{tot},ox}^{i+1}}{C_{agg}^{i+1} - C_{agg}^i} H_{agg}^{i+1} - \dfrac{I_{C_{tot},ox}^i}{C_{agg}^i} H_{agg}^i + I_{H_{tot},ox}^i & \text{if } i = 1 \\[3ex] \dfrac{I_{C_{tot},ox}^{i+1}}{C_{agg}^{i+1} - C_{agg}^i} H_{agg}^{i+1} - \dfrac{I_{C_{tot},ox}^i}{C_{agg}^i - C_{agg}^{i-1}} H_{agg}^i + I_{H_{tot},ox}^i & \text{if } 1 < i < n_{sec} \\[3ex] -\dfrac{I_{C_{tot},ox}^i}{C_{agg}^i - C_{agg}^{i-1}} H_{agg}^i + I_{H_{tot},ox}^i & \text{if } i = n_{sec} \end{cases}$$

$$(77)$$

2.13 Surface reactions model

The heterogeneous surface reactions are described by hydrogen-abstraction-acetylene-addition (HACA) mechanism [18, 36]. The soot growth in HACA scheme is based on a sequential process similar to PAH growth. The hydrogenated arm-chair sites ($C_{soot} - H$) on the edge of aromatic rings are dehydrogenated by H abstraction forming $C_{soot}°$ that bonds with C_2H_2 resulting in an additional aromatic ring with hydrogenated site. These sites can also be attacked by O_2 or OH. The elementary reactions that describe this sequential process are listed in Table 2. The rate of mass growth by HACA is obtained from the reaction of C_2H_2 with dehydrogenated sites as:

$$\omega_{gr}^i = \alpha^i k_{f4} [C_2H_2][C_{soot}°], \tag{78}$$

where k_{f4} denotes the forward rate of Reaction 2 in Table 2, and $[C_{soot}^i°]$ is obtained by multiplying the surface density of dehydrogenated sites, $\chi_{soot}°$ with total surface area of soot (per unit of mass of gas mixture) as:

$$[\mathrm{C}^{\mathrm{i}}_{\mathrm{soot}^\circ}] = \frac{\rho}{Av} A^i_{tot} \cdot \chi_{soot^\circ}, \tag{79}$$

where $\chi_{\mathrm{soot}^\circ}$ is calculated by assuming the steady-state for $[\mathrm{C}_{\mathrm{soot}^\circ}]$ in the system of reactions in Table 2.

$$\chi_{soot^\circ} = \frac{k_{f1}[\mathrm{H}] + k_{f2}[\mathrm{OH}]}{k_{r1}[\mathrm{H_2}] + k_{r2}[\mathrm{H_2O}] + k_{f3}[\mathrm{H}] + k_{f4}[\mathrm{C_2H_2}] + k_{f5}[\mathrm{O_2}] + k_{f1}[\mathrm{H}] + k_{f2}[\mathrm{OH}]} \chi_{soot_{CH}}, \tag{80}$$

where $\chi_{\mathrm{soot_{CH}}}$ is the surface density of hydrogenated sites estimated based on the assumption that soot "surface is assumed to be composed of outwardlooking PAH edges with PAH molecular moieties assembled into turbostratic structures"" [92]. Considering the layer spacing of 3.15Å and 2 C–H bonds per benzene ring length, the surface density of hydrogenated sites, χ_{soot-H}, is calculated to be $0.23\,\mathrm{site/Å^2} = 2.3 \times 10^{19}\mathrm{site/m^2}$, which gives the maximum theoretical limit of the reaction sites.

In Equation (78), α is the surface reactivity factor between 0 and 1 that represents the decline of reaction sites from the theoretical limit due to PAH layer orientation, particle aging, growth and maturity [93, 94], and it has been observed to depend on temperature time history [95, 38]. The value of α has been described using constant target-specific values as well as empirical equations based on particle size and flame temperature. A detailed review of these can be found in the chapter 4 of [96]. Here, the empirical equations proposed by Appel et al. [36] is used to calculate α:

$$\alpha^i = \tanh\left(\frac{12.56 - 0.00563 \cdot T}{\log_{10}\left(\frac{\rho_{soot} \cdot Av}{W_{carbon}} \frac{\pi}{6} d_p^{i\,3}\right)} - 1.38 + 0.00068 \cdot T\right). \tag{81}$$

Alternatively, Blanquart and Pitsch [34] related α to the number of surface hydrogen atoms on the soot particles.

$$\alpha^i = \frac{H^i_{tot}}{C^i_{tot}}. \tag{82}$$

The contribution of HACA to growth source terms can be computed from HACA rates considering the number of carbon atoms in $\mathrm{C_2H_2}$ and number of arm-chair and zig-zag hydrogenated sites on soot particle [56] using

$$I^i_{C_{tot},gr} = 2\omega^i_{gr}/\rho, \tag{83}$$

$$I^i_{H_{tot},gr} = 0.25\omega^i_{gr}/\rho. \tag{84}$$

The rate of change of $\mathrm{C_2H_2}$ concentration due to mass growth is written as:

$$\left(\frac{d[\mathrm{C_2H_2}]}{dt}\right)_{gr} = -\sum_{i=1}^{n_{sec}} \omega^i_{gr}. \tag{85}$$

The rate of release of H radicals into the gas mixture due to surface growth is:

$$\left(\frac{d[\mathrm{H}]}{dt}\right)_{gr} = 1.75 \sum_{i=1}^{n_{sec}} \omega^i_{gr}. \tag{86}$$

The carbons on the surface of soot are oxidized via reaction with $\mathrm{O_2}$ and OH which decreases total carbon of soot and releases CO and $\mathrm{H_2}$ to gas mixture. The oxidation process is described by HACA mechanism. $\mathrm{O_2}$ and OH oxidation rates are calculated as

$$\omega^i_{ox,O_2} = \alpha^i k_{f5}[\mathrm{O_2}][C^i_{soot^\circ}], \tag{87}$$

$$\omega^i_{ox,OH} = \alpha^i k_{f6}[\mathrm{OH}][soot^i]. \tag{88}$$

Table 2: Rate coefficients for the various surface reactions in Arrhenius form $k = AT^n \cdot e^{-E/RT}$

No.	Reaction		A $\left[\frac{m^3}{mol \cdot s}\right]$	n	$\frac{E}{R}$[K]
(R 1)	$C_{soot-H} + H \rightleftharpoons C_{soot°} + H_2$	f	4.17×10^7	0	6542.52
		r	3.9×10^6	0	5535.98
(R 2)	$C_{soot-H} + OH \rightleftharpoons C_{soot°} + H_2O$	f	10^4	0.734	719.68
		r	3.68×10^2	1.139	8605.94
(R 3)	$C_{soot°} + H \longrightarrow C_{soot} + H_2O$	f	10^4	0.734	719.68
(R 4)	$C_{soot°} + C_2H_2 \longrightarrow C_{soot-H}$	f	80	1.56	1912.43
(R 5)	$C_{soot°} + O_2 \longrightarrow 2\,CO$	f	2.2×10^6	0	3774.53
(R 6)	$C_{soot-H} + OH \longrightarrow CO + \frac{1}{2}H_2$	f	1.3×10^7	0	0

The oxidation source term is calculated considering the number of carbon atoms removed from soot through each oxidation pathway as

$$I^i_{C_{tot},ox} = -(2\omega^i_{ox,O_2} + \omega^i_{ox,OH})/\rho. \tag{89}$$

We assume that oxidation does not change the number of surface hydrogen atoms. The rate of change of concentration of CO, H and OH by oxidation is calculates as:

$$\left(\frac{d\,[CO]}{dt}\right)_{ox} = \sum_{i=1}^{n_{sec}} \omega^i_{ox,O_2}. \tag{90}$$

$$\left(\frac{d\,[O_2]}{dt}\right)_{ox} = -\sum_{i=1}^{n_{sec}} \omega^i_{ox,O_2}. \tag{91}$$

$$\left(\frac{d\,[OH]}{dt}\right)_{ox} = -\sum_{i=1}^{n_{sec}} \omega^i_{ox,OH}. \tag{92}$$

$$\left(\frac{d\,[H_2]}{dt}\right)_{ox} = \frac{1}{2}\sum_{i=1}^{n_{sec}} \omega^i_{ox,OH}. \tag{93}$$

2.14 PAH growth models

Here, four different PAH growth models are used to describe the conversion of PAHs to incipient particles and their adsorption on existing agglomerates. As mentioned before, the soot inception and surface growth are not fully understood yet, but there is substantial evidence to support the collision of PAHs as a key step in inception and surface growth [97, 33, 98]. So, global inception models have been developed based PAH collision consisting of different pathways with single or multiple steps. The collision frequency of gaseous species including PAH molecules and polymers depend on their mass and diameter, and it is obtained as:

$$\beta_{dim_{jk}} = 2.2 \cdot d_r^2 \sqrt{\frac{8\pi k_B T}{m_r}} \tag{94}$$

where $d_{r,PAH}$ and $m_{r,PAH}$ are reduced diameter and mass for two PAH molecules, respectively.

$$d_{r,PAH} = 2\frac{d_{PAH_k} \cdot d_{PAH_j}}{d_{PAH_k} + d_{PAH_k}} \tag{95}$$

$$m_{r,PAH} = \frac{m_{PAH_k} \cdot m_{PAH_k}}{m_{PAH_j} + m_{PAH_j}} \tag{96}$$

The mass of each PAH molecule is obtained from its molecular weight as:

$$m_{PAH_j} = \frac{W_{PAH_j}}{Av} \tag{97}$$

The diameter of PAH is calculated from its mass and density.

$$d_{PAH_j} = \left(\frac{6 \cdot m_{PAH_j}}{\pi \cdot \rho_{PAH_j}}\right)^{1/3} \tag{98}$$

The density of a PAH molecule is estimated using the relation proposed by Johansson et al. [99].

$$\rho_{PAH_j} = 171943.5197\frac{W_{carbon} \cdot n_{C,PAH_j} + W_{hydrogen} \cdot n_{H,PAH_j}}{n_{C,PAH_j} + n_{H,PAH_j}} \tag{99}$$

The collision frequency of PAH$_j$ and soot agglomerates in each section can be determined for the entire regime by harmonic mean of the collision frequency in the free molecular and continuum regimes as:

$$\beta^i_{ads_j} = \frac{\beta^i_{fm,ads} \cdot \beta^i_{cont,ads}}{\beta^i_{fm,ads} + \beta^i_{cont,ads}} \tag{100}$$

$$\beta^i_{fm,ads_j} = 2.2\sqrt{\frac{\pi k_B T}{2}\left(\frac{1}{m^i_{agg}} + \frac{1}{m_{PAH_j}}\right)}\left(d^i_g + d_{PAH}\right)^2 \tag{101}$$

$$\beta^i_{cont,ad_js} = \frac{2k_B T}{3\mu}\left[\frac{C^i(d_m)}{d^i_g} + \frac{C^i(d_{PAH_j})}{d_{PAH_j}}\right]\left(d_g + d_{PAH_j}\right) \tag{102}$$

where C^i is the Cunningham function calculated as Equation (33).

2.15   Irreversible Dimerization

The irreversible dimerization is based on the irrversible collision of PAHs leading to their clustering/polymerization that forms dimers, trimers, and tetramers until the polymer mass reaches a threshold that can be considered a solid particle. For practical purposes, dimer is usually considered as a incipient particle that grows by surface growth and coagulation. A single-step irreversible collision of two similar PAHs forms a new dimer as:

$$\text{PAH}_j + \text{PAH}_j \xrightarrow{k_{f,dim_j}} \text{Dimer}_j \tag{R 7}$$

Similarly, the adsorption of each PAH molecule on soot particles is described by the irreversible collision of soot and PAH$_j$ as:

$$\text{PAH}_j + \text{Soot} \xrightarrow{k_{f,ads_j}} \text{Soot} - \text{PAH}_j \tag{R 8}$$
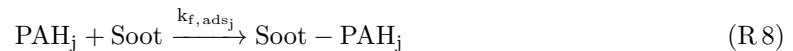
The forward rate of dimerization, k_{f,dim_j} and adsorption, k_{f,ads_j} in Reactions (R 7) and (R 8) are calculated from Equations (94) and (100), respectively.

$$k_{f,dim_j} = \gamma_{inc} \cdot \beta_{jk,PAH} \cdot Av, \tag{103}$$

$$k^i_{f,ads_j} = \gamma_{ads_j} \cdot \beta^i_{j,ads} \cdot Av, \tag{104}$$

where γ_{inc} and γ_{ads} are the collision efficiencies for dimerization and adsorption, respectively. Their value vary in the range of 10^{-7} to, and usually chosen to match the predicted soot mass (volume fraction or size distribution) with the experimental data. Here, $\gamma_{\mathrm{inc}} = 10^{-4}$ and $\gamma_{\mathrm{ads}} = 10^{-3}$. The rate of dimerization and adsorption from PAH$_j$ are calculated accordingly as:

$$w_{dim_j} = \eta_{inc} k_{f,dim_{jj}} [\mathrm{PAH_j}][\mathrm{PAH_j}], \tag{105}$$

where η_{inc} is the inception adjustment factor to globally modify the inception flux without changing the internal rate constants of the inception model. The partial source terms for inception are calculated as:

$$I_{N,inc} = \frac{1}{\rho} \sum_{j=1}^{n_{PAH}} w_{dim_j} 2n_{PAH_j,C} \tag{106}$$

$$I_{C_{tot},inc} = \frac{1}{\rho} \sum_{j=1}^{n_{PAH}} w_{dim_j} 2n_{PAH_j,C} \tag{107}$$

$$I_{H_{tot},inc} = \frac{1}{\rho} \sum_{j=1}^{n_{PAH}} w_{dim_j} 2n_{PAH_j,H} \tag{108}$$

The rate of PAH adsorption for each section is obtained as:

$$w^i_{ads_j} = \eta_{ads} k^i_{f,ads_j} [\mathrm{soot}][\mathrm{PAH_j}], \tag{109}$$

where η_{ads} is the adsorption adjustment factor to globally modify the PAH adsorption rate. The contribution of PAH adsorption to the source terms are expressed as:

$$I^i_{C_{tot},ads} = \frac{1}{\rho} \sum_{j=1}^{n_{PAH}} w^i_{ads_j} n_{PAH,C} \tag{110}$$

$$I^i_{H_{tot},ads} = \frac{1}{\rho} \sum_{j=1}^{n_{PAH}} w^i_{dim_j} (n_{PAH,H} - 2) \tag{111}$$

Each PAH molecule loses one H atom becoming a radical that forms bonds with a dehydrogenated site on soot surface, so two H atoms are released during the process that is taken into account in Equation (111).

The formation of a dimer consumes two PAH molecules, and during adsorption one PAH molecule is removed from the gas mixture, so the total rate of PAH$_i$ removal by the irreversible dimerization is obtained as:
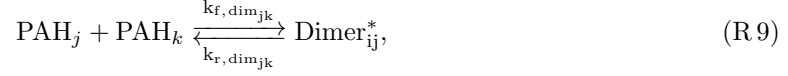
$$\left(\frac{d[\mathrm{PAH_j}]}{dt} \right)_{inc} = -2w_{dim_j} - \sum_{i=1}^{n_{sec}} w^i_{ads_j}. \tag{112}$$

During the adsorption process one H$_2$ is released to the gas mixture.

$$\left(\frac{d[\mathrm{H_2}]}{dt} \right)_{inc} = \sum_{i=1}^{n_{sec}} w^i_{ads_j}. \tag{113}$$

22

2.16   Reactive Dimerization

This model is built on Irreversible Dimerization with two main differences: The first step of dimerization and adsorption is reversible forming physically bonded dimers followed by a irreversible carbonization that leads to chemical bond formation in dimers [31]. This approach allows formation of homo- and heterodimers. The dimerization of PAH_j and PAH_k is described as:

$$PAH_j + PAH_k \xrightleftharpoons[k_{r,dim_{jk}}]{k_{f,dim_{jk}}} Dimer_{ij}^*, \tag{R 9}$$

$$Dimer_{jk}^* \xrightarrow{k_{reac}} Dimer_{jk}, \tag{R 10}$$

where $Dimer_{jk}^*$ and $Dimer_{jk}$ physically and chemically bonded dimers, respectively, from PAH_j and PAH_k. The forward rate of physical dimerization, $k_{f,dim_{jk}}$ is calculated from Equation (94) as:

$$k_{f,dim_{jk}} = p'' \cdot \beta_{jk,PAH} \cdot Av, \tag{114}$$

where $p'' = 0.1$ accounts for the probability of PAH-PAH collisions in "FACE" configuration that results in successful vdW bond formation [100]. The reverse rate of physical dimerization, $k_{r,dim_{jk}}$ is obtained from the dimerization equilibrium constant [101] as:

$$\log_{10} K_{eq} = a\frac{\epsilon_{jk}}{RT} + b, \tag{115}$$

$$k_{r,dim_{jk}} = k_{f,dim_{jk}} 10^{-b} e^{-a\epsilon_{jk} ln(10)/(RT)}, \tag{116}$$

$$\epsilon_{jk} = cW_{jk} - d, \tag{117}$$

$$W_{jk} = \frac{W_j \cdot W_k}{W_j + W_k}, \tag{118}$$

where $a = 0.115$ (obtained from pyrere dimerization data [26]) and b=1.8 [31], c=933420 j/kg, and d=34053 j/mol [31].

The rate of chemical bond formation, k_{reac} is defined in the Arrhenius form [27] as

$$k_{reac} = 5 \times 10^6 \cdot e^{(-96232/RT)}. \tag{119}$$

Assuming a steady state condition for the physical dimers, $\partial[Dimer_{jk}^*]/\partial t = 0$, the rate of formation of chemically-bonded dimers can be obtained as

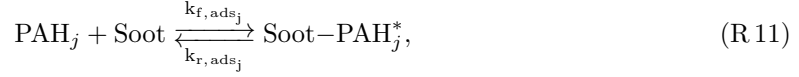$$\omega_{dim_{jk}} = \eta_{inc} k_{reac} \frac{k_{f,dim_{jk}}[PAH_j][PAH_k]}{k_{r,dim_{jk}} + k_{c,dim}}. \tag{120}$$

The contribution of dimer formation to partial source terms is expressed by looping over all combinations of PAHs as:

$$I_{N,inc} = \frac{1}{\rho} \sum_{j=1}^{n_{PAH}} \sum_{k=j}^{n_{PAH}} \omega_{dim_{kj}} \left(n_{PAH_j,C} + n_{PAH_k,C} \right), \tag{121}$$

$$I_{C_{tot},inc} = \frac{1}{\rho} \sum_{j=1}^{n_{PAH}} \sum_{k=j}^{n_{PAH}} \omega_{dim_{kj}} \left(n_{PAH_j,C} + n_{PAH_k,C} \right), \tag{122}$$

$$I_{H_{tot},inc} = \frac{1}{\rho} \sum_{j=1}^{n_{PAH}} \sum_{k=j}^{n_{PAH}} \omega_{dim_{kj}} \left(n_{PAH_j,H} + n_{PAH_k,H} \right), \tag{123}$$

Similarly, PAH adsorption is described by a two-step process where the collision of PAH_j with soot agglomerates leads to physically bonded $Soot - PAH^*$ that is carbonized and forms chemically-bonded $Soot - PAH$ added to soot surface.

$$PAH_j + Soot \underset{k_{r,ads_j}}{\overset{k_{f,ads_j}}{\rightleftharpoons}} Soot-PAH_j^*, \tag{R 11}$$

$$Soot-PAH_j^* \xrightarrow{k_{c,ads}} Soot-PAH_j, \tag{R 12}$$
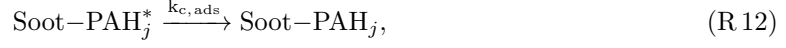
The forward rate of PAH-soot collision is calculated from Equation (100), and the reverse rate is determined same as inception (Equation(116)).

$$k_{f,ads}^i = \beta_{jk,ads}^i \cdot Av, \tag{124}$$

$$k_{r,ads}^i = k_{f,ads}^i \cdot 10^{-b} e^{-a\epsilon_{soot,j}\ln(10)/(RT)}, \tag{125}$$

$$\epsilon_{soot,j} = cW_{soot,j} - d, \tag{126}$$

a, b, c, d values are the same as those used in inception. Computing $\epsilon_{soot,j}$ also requires "equivalent soot molecular weight", W_{soot} for section i, which is estimated from carbon mass of each agglomerate as:

$$W_{soot}^i = \frac{C_{tot}^i W_{carbon}}{N_{agg}^i} \tag{127}$$

The rate constant of carbonization of $Soot - PAH_j^*$ is defined as in the Arrhenius form similar to inception (Equation (119)). The prefactor is adjusted based on matching the numercial PSD [27] with measurements in the ethylene pyrolysis in a flow reactor [102].

$$k_{c,dim} = 2 \times 10^{10} \cdot e^{(-96232/RT)}. \tag{128}$$

The total adsorption rate can be calculated assuming a steady-state concentration for physically adsorbed PAH on soot, $\partial[Soot - PAH^*]/\partial t = 0$ calculated in a similar way to inception flux (Equation (120)) as

$$\omega_{ads_j}^i = \eta_{ads}k_{c,ads}\frac{k_{f,ads_j}[Soot][PAH_j]}{k_{r,ads_j} + k_{c,ads_j}}, \tag{129}$$

The contribution of PAH adsorption rate to partial source terms can be expressed as:

$$I_{C_{tot},ads}^i = \frac{1}{\rho} \sum_{i=1}^{n_{PAH}} \omega_{ads_j}^i n_{C,PAH_j}, \tag{130}$$

$$I_{C_{tot},ads}^i = \frac{1}{\rho} \sum_{i=1}^{n_{PAH}} \omega_{ads_j}^i \left(n_{H,PAH_j} - 2\right). \tag{131}$$

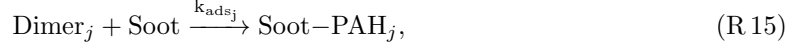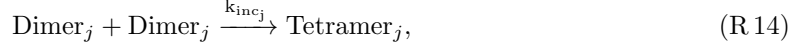The rate of removal of PAH from gas mixture due to adsorption is given as

$$\left(\frac{d[PAH_j]}{dt}\right)_{inc} = - \sum_{k=1}^{n_{PAH}} w_{dim_{jk}} - \sum_{i=1}^{n_{sec}} w_{ads_j}^i. \tag{132}$$

During the adsorption process one H_2 is released to the gas mixture.

$$\left(\frac{d[H_2]}{dt}\right)_{inc} = \sum_{i=1}^{n_{sec}} w_{ads_j}^i. \tag{133}$$

24

2.17 Dimer Coalescence

Dimer coalescence model is a multi-step irreversible model proposed by Blanquart and Pitsch [34] where self-collision of PAH molecules form dimers that are intermediate state between gaseous PAH molecules and solid soot particles. The self-coalescence of dimers forms incipient soot particles. Alternatively, dimers can adsorb on the surface of existing soot particles and contribute to their surface growth. The equations are based on implementation of Dimer Coalescence by Sun et al. [103] for a sectional model.

$$\text{PAH}_j + \text{PAH}_j \xrightarrow{\text{k}_{\text{dim}_j}} \text{Dimer}_j, \tag{R 13}$$

$$\text{Dimer}_j + \text{Dimer}_j \xrightarrow{\text{k}_{\text{inc}_j}} \text{Tetramer}_j, \tag{R 14}$$

$$\text{Dimer}_j + \text{Soot} \xrightarrow{\text{k}_{\text{ads}_j}} \text{Soot}-\text{PAH}_j, \tag{R 15}$$

where the rate constant of dimerization, k_{dim_j} and inception k_{inc_j} are calculated from collision rate of PAHs in Equation (100).

$$k_{dim_j} = \gamma_{dim_j} \cdot \beta_{jj,PAH} \cdot Av, \tag{134}$$

$$k_{inc_j} = \beta_{jj,dimer} \cdot Av, \tag{135}$$

where γ_{dim_j} is the dimerization efficiency that is assumed to scale with fourth power of PAH molecular weight [56] as:

$$\gamma_{dim_j} = C_{N,j} \cdot W^4_{PAH_j}, \tag{136}$$

Blanquart and Pitsch [34] estimated the constant $C_{N,j}$ by comparing the profiles of several PAH species with experimental measurements in a single premixed benzene flame [104], and provided a efficiency values for various PAHs that are listed in Table 1 in [56]. The rate of dimer collision is expressed as:

$$w_{dim_j} = \eta_{inc}k_{inc_j}[\text{Dimer}_\text{j}][\text{Dimer}_\text{j}] \tag{137}$$

Similarly, the rate of adsorption of dimers on soot particles is obtained as:

$$w^i_{ads_j} = \eta_{ads}k^i_{ads_j}[\text{soot}]^i[\text{Dimer}_\text{j}] \tag{138}$$

Assuming fast dimer consumption leads to the steady-state concentration of dimers that can be determined by solving a quadratic equation as:

$$a_{inc_j}[\text{dimer}]^2 + b_{ads_j}[\text{dimer}] = \omega_{dim,j} \tag{139}$$

$$[\text{Dimer}_\text{j}] = \begin{cases} \dfrac{-b_{ads_j} + \sqrt{\Delta_j}}{2a_{inc_j}}, & \text{if } \Delta_j \geq 0 \\ 0 & \text{if } \Delta_j < 0 \end{cases} \tag{140}$$

$$\Delta_j = b^2_{ads_j} - 4a_{inc_j}\omega_{dim,j} \tag{141}$$

where $a_{inc_j} = k_{inc_j}$ and b_{ads_j} is calculated by summing the adsorption rate of dimer for all sections and dividing it by the dimer concentration.

$$\text{b}_{\text{ads}_\text{j}} = \sum_{i=1}^{n_{sec}} k^i_{ads_j}[\text{soot}]^i \tag{142}$$

After determining the concentration of each dimer, the contribution of inception and PAH adsorption to source terms of tracked soot variables can be calculated similar to previous inception models considering the number of carbon and hydrogen atoms involved in the process.

$$I_{N,inc} = \frac{1}{\rho} \sum_{j=1}^{n_{PAH}} 4\omega_{inc_j} n_{PAH_j,C}, \tag{143}$$

$$I_{C_{tot},inc} = \frac{1}{\rho} \sum_{j=1}^{n_{PAH}} 4\omega_{inc_j} n_{PAH_j,C}, \tag{144}$$

$$I_{H_{tot},inc} = \frac{1}{\rho} \sum_{j=1}^{n_{PAH}} 4\omega_{inc_j} \left(n_{PAH_j,H} - 2 \right), \tag{145}$$

$$I_{C_{tot},ads}^{i} = \frac{1}{\rho} \sum_{i=1}^{n_{PAH}} 2\omega_{ads_j}^{i} n_{C,PAH_j}, \tag{146}$$

$$I_{C_{tot},ads}^{i} = \frac{1}{\rho} \sum_{i=1}^{n_{PAH}} 2\omega_{ads_j}^{i} \left(n_{H,PAH_j} - 2 \right). \tag{147}$$

The rate of removal of PAHs and release of H$_2$ due to inception and PAH adsorption is calculated as:

$$\left(\frac{d\,[\mathrm{PAH_j}]}{dt} \right)_{inc} = -4 \sum_{k=1}^{n_{PAH}} w_{inc_j} - 2 \sum_{i=1}^{n_{sec}} w_{ads_j}^{i}. \tag{148}$$

$$\left(\frac{d\,[\mathrm{H_2}]}{dt} \right)_{inc} = 2 \sum_{i=1}^{n_{sec}} w_{ads_j}^{i}. \tag{149}$$

2.18 E-Bridge Modified

The E-Bridge Formation was originally proposed by Frenklach and Mebel [32] to describe soot inception using a HACA-like scheme that starts with dehydrogenation of PAH monomers, often pyrene, which forms the monomer radicals and continues with of sequential addition of the radicals to PAHs that form dimers, trimers and larger polymers until the PAH structure reaches the mass threshold and the clustering process becomes irreversible. Here, a modified version of EBridge Formation model is used where dimers are considered as incipient soot, and monomer radical are adsorbed on soot agglomerates. This PAH growth model is described using the following set of pathways:

$$\mathrm{PAH}_j + \mathrm{H} \underset{\mathrm{k_{r,d_j}}}{\overset{\mathrm{k_{f,d_j}}}{\rightleftharpoons}} \mathrm{P\dot{A}H_j} + \mathrm{H_2}, \tag{R 16}$$

$$\mathrm{P\dot{A}H_j} + \mathrm{H} \xrightarrow{\mathrm{k_{f,h_j}}} \mathrm{PAH}_j, \tag{R 17}$$

$$\mathrm{P\dot{A}H_j} + \mathrm{PAH}_j \xrightarrow{\mathrm{k_{inc_j}}} \mathrm{Dimer}_j, \tag{R 18}$$

$$\mathrm{P\dot{A}H_j} + \mathrm{Soot} \xrightarrow{\mathrm{k_{ads_j}}} \mathrm{Soot{-}PAH}_j, \tag{R 19}$$
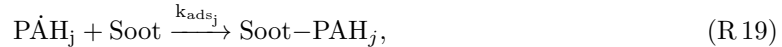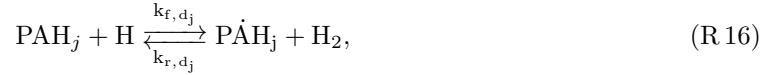
The rate constants of Reactions (R 16)&(R 17) are listed in Table 3 while those of dimer production and adsorption are calculated based on Equations (94)&(100), respectively. For both steps, it is assumed the all collisions are successful i.e. 100% collision efficiency for radical-monomer and radical-soot.

$$k_{inc_j} = \beta_{jj,PAH} \cdot Av, \tag{150}$$

$$k_{ads_j}^{i} = \beta_{ads_j}^{i} \cdot Av, \tag{151}$$

Table 3: Rate coefficients for the monomer de-/hydrogenation reaction of E-Bridge Modified in Arrhenius form $k = AT^n \cdot e^{-E/RT}$ [32]

Reaction		A $\left[\frac{m^3}{mol \cdot s}\right]$	n	$\frac{E}{R}$[K]
(R 16)	f	$98\times n_{C,PAH_j}$	1.8	7,563.519
	r	1.6×10^{-2}	2.63	2145.346
(R 17)	f	4.8658×10^7	0.13	0.0

The rate of dimer formation and adsorption is calculated as:

$$w_{dim_j} = \eta_{inc} k_{inc_j}[PAH_j][P\dot{A}H_j] \tag{152}$$

$$w^i_{ads_j} = \eta_{ads} k^i_{ads_j}[Soot]^i[P\dot{A}H_j] \tag{153}$$

The calculations of rate of inception and PAH adsorption from PAH_j requires the concentration of corresponding monomer radical that can be determined by applying the steady-state assumption for $P\dot{A}H_j$.

$$\frac{d[P\dot{A}H_j]}{dt} = 0$$

$$k_{f,d_j}[PAH_j][H] - k_{r,d_j}[P\dot{A}H_j][H_2] - k_{f,h_j}[P\dot{A}H_j][H] - k_{inc_j}[P\dot{A}H_j]^2$$
$$- \sum_{i=1}^{n_{sec}} k^i_{ads_j}[P\dot{A}H_j][Soot]^i = 0$$

The above equations can be rearranged as a quadratic equation similar to the dimer coalescence.

$$a_{inc_j}[P\dot{A}H_j]^2 + b_{ads_j}[P\dot{A}H_j] + c_j = 0, \tag{154}$$

$$a_{inc_j} = k_{f,d_j} \tag{155}$$

$$b_{ads_j} = k_{r,d_j}[H_2] + k_{f,h_j}[H] + \sum_{i=1}^{n_{sec}} k^i_{ads_j}[Soot]^i \tag{156}$$

$$c_{inc_j} = k_{f,d_j}[PAH_j][H] \tag{157}$$

Finally, solving the quadratic equation for each PAH results in concentration of the radical using the following equation as:

$$[P\dot{A}H_j] = \begin{cases} \dfrac{-b_{ads_j} + \sqrt{\Delta_j}}{2a_{inc_j}}, & \text{if } \Delta_j \geq 0 \\ 0 & \text{if } \Delta_j < 0 \end{cases} \tag{158}$$

$$\Delta_j = b^2_{ads_j} - 4a_{inc_j}c_j \tag{159}$$

The contribution of inception and adsorption to the partial source terms for E-Bridge Modified can be written as:

$$I_{N,inc} = \frac{1}{\rho} \sum_{j=1}^{n_{PAH}} 2\omega_{inc_j} n_{PAH_j,C}, \tag{160}$$

$$I_{C_{tot},inc} = \frac{1}{\rho} \sum_{j=1}^{n_{PAH}} 2\omega_{inc_j} n_{PAH_j,C}, \tag{161}$$

$$I_{H_{tot},inc} = \frac{1}{\rho} \sum_{j=1}^{n_{PAH}} 2\omega_{inc_j} \left(n_{PAH_j,H} - 2 \right), \tag{162}$$

$$I_{C_{tot},ads}^i = \frac{1}{\rho} \sum_{i=1}^{n_{PAH}} \omega_{ads_j}^i n_{C,PAH_j}, \tag{163}$$

$$I_{C_{tot},ads}^i = \frac{1}{\rho} \sum_{i=1}^{n_{PAH}} \omega_{ads_j}^i \left(n_{H,PAH_j} - 2 \right). \tag{164}$$

The rate of removal of each PAH involved in soot inception and PAH adsorption and release of H_2 to the gas mixture can be expressed as:

$$\left(\frac{d\,[\mathrm{PAH_j}]}{dt} \right)_{inc} = -2 \sum_{k=1}^{n_{PAH}} w_{inc_j} - \sum_{i=1}^{n_{sec}} w_{ads_j}^i. \tag{165}$$

$$\left(\frac{d\,[\mathrm{H_2}]}{dt} \right)_{inc} = \sum_{i=1}^{n_{sec}} w_{ads_j}^i. \tag{166}$$

2.19 Gas scrubbing rates

The rate of production/destruction of species involved in soot formation must be taken into account to preserve the mass and energy balance in reactive systems. In order to do that, the production rate of gaseous species calculated by Cantera must be corrected for the rate of release/consumption due to PAH growth and surface reaction models.

$$\left(\frac{d\,[\mathrm{PAH_j}]}{dt} \right)_{tot} = \left(\frac{d\,[\mathrm{PAH_j}]}{dt} \right)_{gas} + \left(\frac{d\,[\mathrm{PAH_j}]}{dt} \right)_{inc} + \left(\frac{d\,[\mathrm{PAH_j}]}{dt} \right)_{ads}. \tag{167}$$

H_2 is released to the gas mixture due to inception, PAH adsorption as well as oxidation.

$$\left(\frac{d\,[\mathrm{H_2}]}{dt} \right)_{tot} = \left(\frac{d\,[\mathrm{H_2}]}{dt} \right)_{gas} + \left(\frac{d\,[\mathrm{H_2}]}{dt} \right)_{inc} + \left(\frac{d\,[\mathrm{H_2}]}{dt} \right)_{ads} + \left(\frac{d\,[\mathrm{H_2}]}{dt} \right)_{ox}. \tag{168}$$

Surface growth consumes C_2H_2 and adds H_2 to the gas mixture.

$$\left(\frac{d\,[\mathrm{C_2H_2}]}{dt} \right)_{tot} = \left(\frac{d\,[\mathrm{C_2H_2}]}{dt} \right)_{gas} + \left(\frac{d\,[\mathrm{C_2H_2}]}{dt} \right)_{gr}. \tag{169}$$

$$\left(\frac{d\,[\mathrm{H}]}{dt} \right)_{tot} = \left(\frac{d\,[\mathrm{H}]}{dt} \right)_{gas} + \left(\frac{d\,[\mathrm{H}]}{dt} \right)_{gr}. \tag{170}$$

Oxidation uses O_2 and OH to remove carbon from soot particles and generates H_2 and CO.

$$\left(\frac{d\,[\mathrm{CO}]}{dt} \right)_{tot} = \left(\frac{d\,[\mathrm{CO}]}{dt} \right)_{gas} + \left(\frac{d\,[\mathrm{CO}]}{dt} \right)_{ox}. \tag{171}$$

$$\left(\frac{d\,[\mathrm{O2}]}{dt} \right)_{tot} = \left(\frac{d\,[\mathrm{O2}]}{dt} \right)_{gas} + \left(\frac{d\,[\mathrm{O2}]}{dt} \right)_{ox}. \tag{172}$$

$$\left(\frac{d\,[\mathrm{OH}]}{dt} \right)_{tot} = \left(\frac{d\,[\mathrm{OH}]}{dt} \right)_{gas} + \left(\frac{d\,[\mathrm{OH}]}{dt} \right)_{ox}. \tag{173}$$

3 Code Validation

A set of simulations was performed to ensure the accuracy and reliability of omnisoot for prediction of soot formation. Aerosol dynamics is validated by comparing the results of population balance models implemented in omnisoot with those of DEM simulations from literature. Carbon and hydrogen mass and energy balance is also rigorously evaluated to ensure that residuals fall within the bounds of acceptable numerical error.

3.0.1 Collision Frequency

The collision frequency function determines the rate at which two particles collide, which results in the reduction of total number of agglomerates and increase in size. In the absence of strong flow shear or external forces, Brownian motion is the main driving force for particle coagulation. As explained in Sections 2.11.1 & 2.12.1, omnisoot employs harmonic mean and Fuchs interpolations to calculate collision frequency of agglomerates from free-molecular to continuum regimes based on gas mean free path, and particle morphology.

The test case for validation of collision frequency is based on the DEM simulation of 2000 monodisperse spherical particles with the density of 2200 kg/m^3 in a cubic cell with the constant temperature of 298 K and pressure of 1 atm [105]. Figure 7 depicts the collision frequency plotted against Knudsen number ($Kn = 2\lambda/d_m$) obtained by omnisoot using harmonic mean (red solid line) and Fuchs interpolation (green dashed line) and DEM results of Goudeli et al. [105]. The Fuchs interpretation perfectly matches DEM data over the free-molecular ($Kn<10$) to the continuum ($Kn>10$) range. Harmonic mean is also in good agreement with the DEM results in the free-molecular and continuum regime, but slightly underpredicts the collision frequency in the transition regime ($0.1 \leq Kn \leq 10$) with relative errors less than 16%.
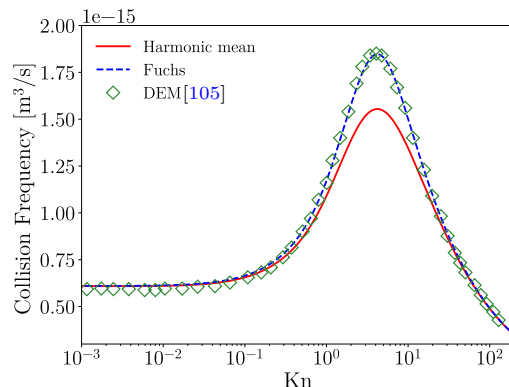
Figure 7: The comparison of collision frequency, β, obtained by omnisoot using harmonic mean (red solid line) and Fuchs interpolation (green dashed line) with DEM results (symbols) [105]

3.1 Coagulation

This test case was designed and conducted to validate the coagulation sub model of both particle dynamics models, MPBM and SPBM, by comparing the results of omnisoot with those of DEM [106]. The constant volume reactor was used for this test case, but it will be applicable to other reactors and flame models as long as the particle residence time matches with the values obtained by DEM. An adiabatic reactor with the volume of 1 m^3 is initialized with 2.6261×10^{18} spherical particles 2 nm in diameter. The initial conditions are indicated in Table 4. The particles are allowed to coagulate in the free molecular regime and grow in size while no inception, PAH adsorption and surface growth occur. Figure 9 demonstrates the number density of agglomerates (N_{agg}) and primary particles (N_{pri}), and mobility (d_m) and gyration (d_m) diameters of particle obtained by omnisoot that are

Table 4: The simulations conditions of the coagulation test case [106]

Property	Value
Composition	CH_4:0.425, O_2:0.435, N_2:0.14
T	1830 K
P	1 atm
N_{agg}^1	3.514×10^{-5}mol/kg
N_{pri}^1	3.514×10^{-5}mol/kg
d_p^1	2 nm

in good agreement with DEM results. N_{pri} is conserved during coagulation resulting in identical flat lines for both particle dynamics models, but N_{agg} declines over time with the higher decay rate for SPBM because it accounts for the polydispersity of agglomerates that results in larger collision frequency compared to MPBM. Therefore, mean mobility and gyration diameter of SPBM (red lines in Fig. 9-b) are slightly larger than those of MPBM (blue line of the same figure).
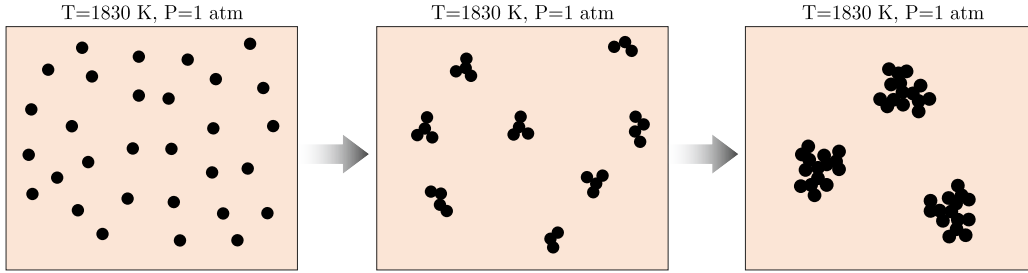
Figure 8: The schematic of agglomeration process in the coagulation test cases where initially spherical particle collide and form agglomerate

MPBM model cannot resolve PSD because of the monodispersity assumption. In contrast, SPBM tracks the number concentration of particles in separate sections that can be used to construct evolving PSD and calculate mean properties and determine the spread of size distribution of particles during coagulation. Figure 10-a shows the standard deviation of mobility diameter, σ_g predicted by SPBM in close agreement with DEM results. σ_g starts from unity indicating a monodisperse population at the beginning of simulation, and it finally reaches 2.03 that is the signature standard deviation of the free molecular regime [107]. Fig. 10 demonstrates the evolution of non-dimensional PSD from t=1 ms to 677 ms. The PSD is plotted for the normalized concentration, $\Psi = \bar{v}n_{agg}(v,t)/N_{agg,\infty}$ and dimensionless volume, $\eta = v/\bar{v}$, where $n_{agg}(v,t)$ is the size distribution function of agglomerate, v particle volume, $\bar{v}$ mean particle volume, $N_{agg,\infty}$ total number concentration of agglomerates. For short residence times, t$\approx$4 ms, the PSD resembles a half bell curve because the majority of particles has sizes close to $d_0 = 2nm$ with the average volume close to the minimum volume, so the particles with $\eta \approx 1$ has the largest concentration. As particles grow by coagulation, the PSD rapidly transitions to a full bell-curve (t $\geq$ 22ms) and does not change for longer residence times, t $\geq$ 447ms marking the attainment of SPSD in a good agreement with DEM results. This confirms the capability of SPBM implemented in omnisoot to capture SPSD for soot agglomerates as a signature of Brownian-driven particle coagulation.
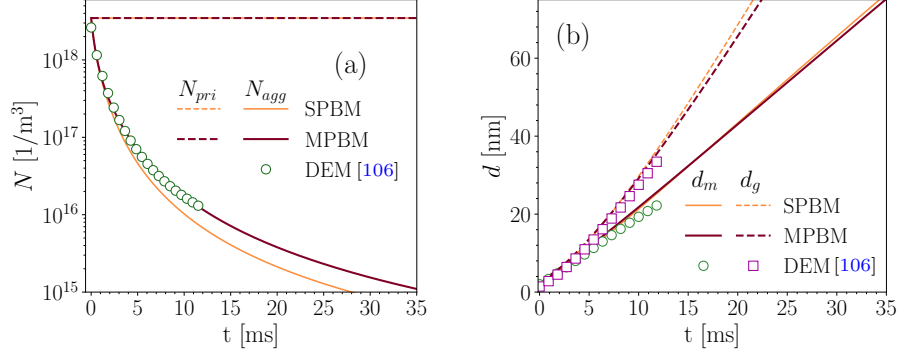
Figure 9: The total number concentration of agglomerates and primary particles (a), and mobility and gyration diameter (b) obtained with omnisoot using MPBM and SPBM that are in close agreement with the DEM results [106] indicating the validation of coagulation sub-model
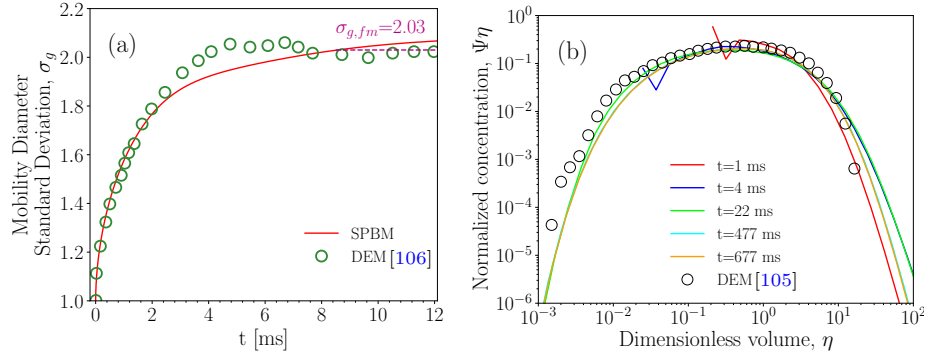

Figure 10: The standard deviation (residual) of mobility diameter, σ_g obtained with SPBM in close agreement with DEM results [106] (left pane) that reaches $\sigma_{g,fm} = 2.03$ characteristic of the free molecular regime [107]; the particle size distribution (normalized number concentration of agglomerates is plotted against non-dimensional volume in the right pane) at different residence times that overlaps after initial transient phase marking the attainment of self-preserving size distribution in good agreement with DEM results [105]

3.2 Constant Volume Reactor

The pyrolysis of 30% CH_4 diluted in N_2 with the initial temperature and pressure of 2455 K and 3.47 atm, respectively, was simulated using the constant volume reactor model in the residence time of 40 ms. The combination of available PAH growth and particle dynamics models leads to eight different cases that were simulated to ensure the conservation of mass and energy. Here, we focus on the total elemental balance of carbon and hydrogen because they are involved in soot processes. Figure 11 demonstrates the relative error of total carbon, hydrogen and energy of system for different PAH growth and particle dynamics models in the constant pressure reactor that is less than 10^{-10} for all parameters confirming the validity of model in satisfying the mass and energy balance.
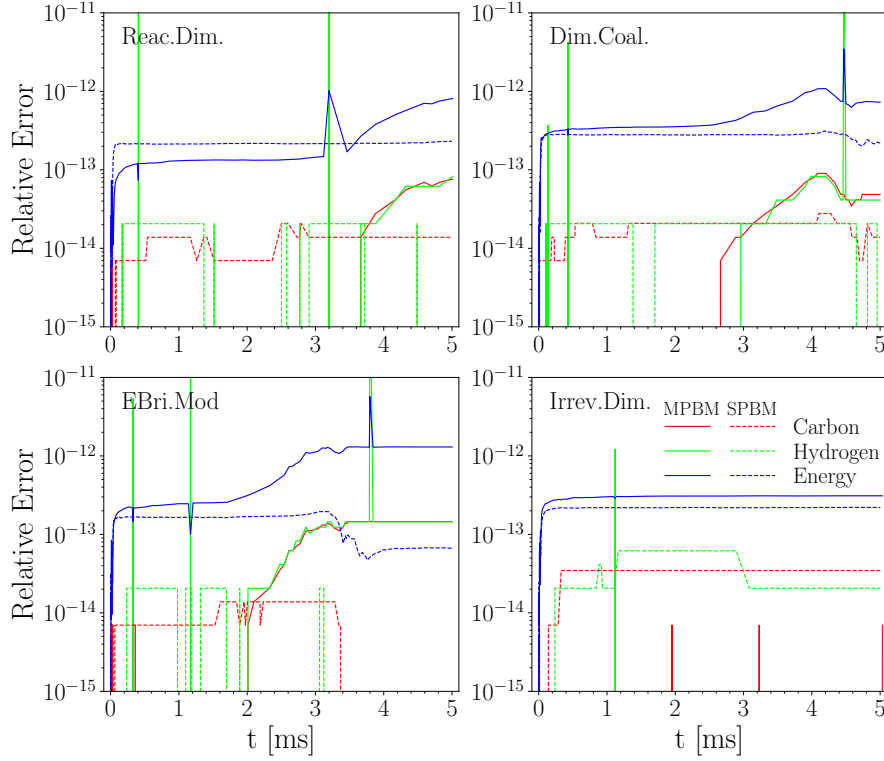
31
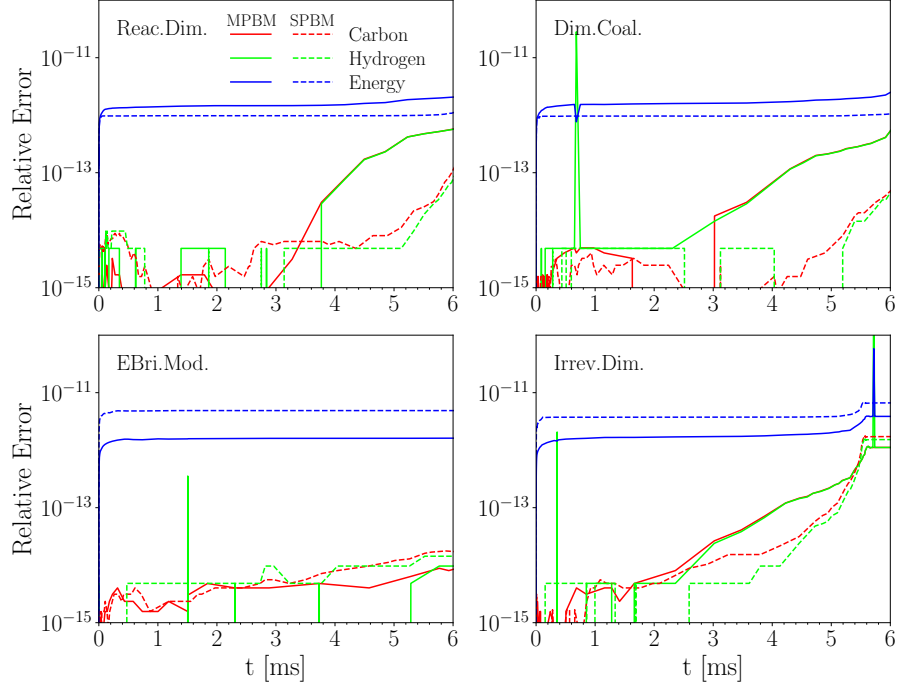
Figure 11: The relative error (residual) of total carbon (red line) and hydrogen (green line) mass, and total internal energy residual of gas and soot (blue line) plotted against residence time during pyrolysis of 30% CH_4-N_2 at 2455 K and 3.47 atm in the constant volume reactor simulated using different PAH growth models along with MPBM (solid line) and SPBM (dashed line)

3.3 Constant Pressure Reactor

The pyrolysis of 5% CH_4-Ar in a shock-tube with post-reflected-shock temperature and pressure of T_5=2355 K and P_5=4.64 atm, respectively, was simulated using CPR model. Figure 12 shows the relative error of total carbon, hydrogen and energy of system for different PAH growth and particle dynamics models in the constant volume that falls below 10^{-10} for all parameters confirming the validity of model in satisfying the mass and energy balance in the constant pressure reactor using all models.
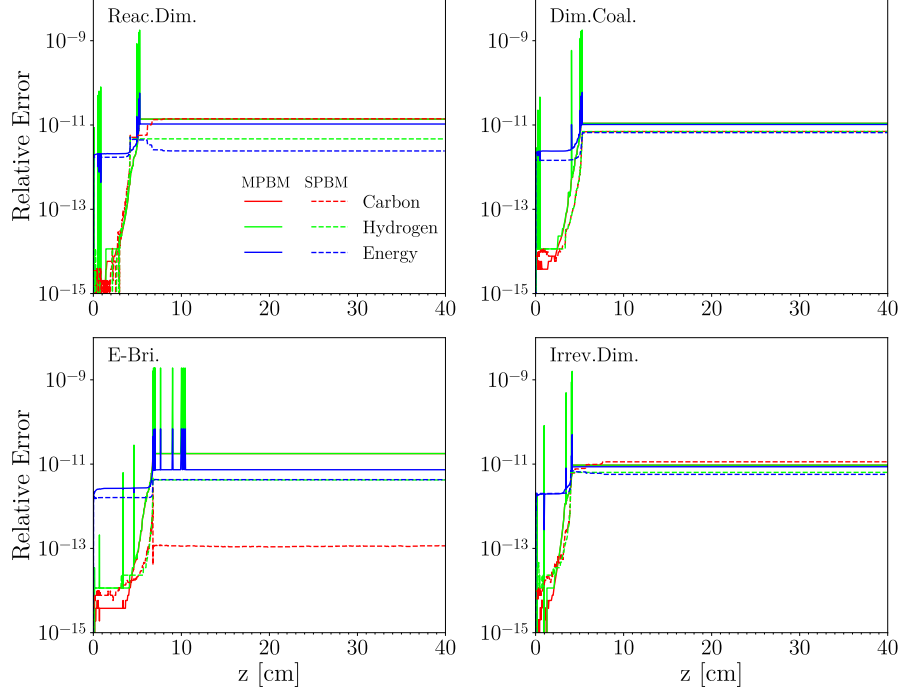
Figure 12: The relative error (residual) of total carbon (red line) and hydrogen (green line) mass, and total internal energy residual of gas and soot (blue line) plotted against residence time during pyrolysis of 5% CH_4-Ar at 2355 K and 4.64 atm simulated using the constant pressure reactor with different PAH growth model, MPBM (solid line) and SPBM (dashed line)

3.4 Plug Flow Reactor

Methane pyrolysis in an adiabatic flow reactor is used to check elemental carbon and hydrogen, and energy balance in the PFR model. The inlet flow enters the reactor at the composition of 30% CH_4 diluted in N_2, and T=2100 K and P=1 atm. Figure 13 shows the residual of total elemental carbon and hydrogen, and energy up to 40 cm of the reactor length using all PAH growth and particle dynamics model. The residuals are in the order of 10^{-11} and start to grow at the beginning of the reactor by pyrolysis of CH_4 and the formation of intermediate species such and C_2H_2 and PAHs. This initiates soot inception of surface growth affecting the gas chemistry and energy that ends near x=10 cm, and then the coagulation of particles is dominant with no affect on mass and energy of particles. As a result, PFR model of omnisoot satisfied the conservation of the mass and energy.
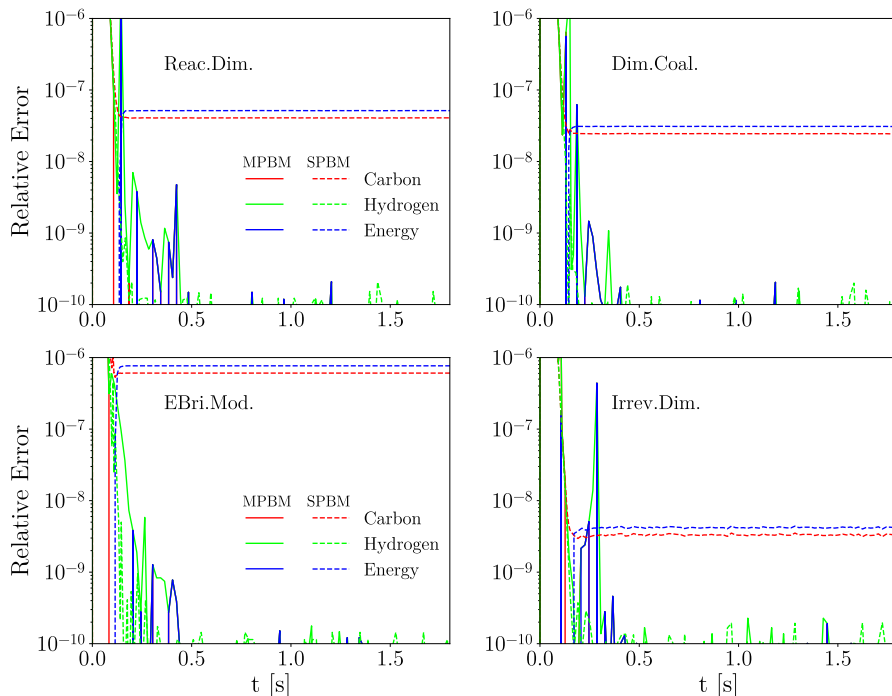
Figure 13: The relative error (residual) of total carbon (red line) and hydrogen (green line) mass, and total internal energy residual of gas and soot (blue line) plotted against reactor length (cm) in the adiabatic flow reactor during pyrolysis of 30% CH_4-N_2 at 2100 K and 1 atm simulated using different PAH growth models and MPBM (solid line) and SPBM (dashed line)

3.5 Perfectly Stirred Reactor

The mass and energy balance are investigated for soot formation during ethylene-air oxidation at $\phi = 2$ in a perfectly stirred reactor. The simulation conditions were chosen based on the combustor implemented and utilized by Stouffer et al. [108]. The reactants initially at 300 K enter a reactor of 250 ml that works under atmospheric pressure. The simulation is initialized from a high temperature (2000 K) to avoid trivial solution (cold reactant leaving the reactor with no chemical reactions) and to ensure the model captures a sustained combustion. The residence time of products in the reactor is 8.5 ms. Figure 14 shows the relative error of total elemental carbon and hydrogen mass and total enthalpy of gas and soot, which is less than 10^{-6} for all combinations of particle dynamics and PAH growth models.

Figure 14: The relative error (residual) of total carbon (red line) and hydrogen (green line) mass, and total internal energy residual of gas and soot (blue line) plotted in simulation time during adiabatic combustion of C_2H_4-air with $\phi = 2$ at 1 atm simulated using different PAH growth models and MPBM (solid line) and SPBM (dashed line)

4   Results and Discussion

The lack of quantitative knowledge about soot inception and surface growth pathways has hindered the development of accurate models for predicting soot mass and morphology. Uncertainties in the gas-phase chemistry of small and large intermediates can result in orders-of-magnitude differences in the predicted concentrations of PAHs. These uncertainties are further amplified by inception models, making soot modeling even more challenging. As a result, the choice of reaction mechanism becomes a critical factor in soot simulations.

A series of simulations were performed using the CPR mode of Omnisoot, excluding soot formation, to highlight the differences among six reaction mechanisms in describing gas-phase chemistry during the pyrolysis of a 10% CH_4-Ar mixture at T_5=2200 K and P_5=4.5 atm. The selected mechanisms include: ABF [36], Caltech [109], KAUST [110], CRECK [111], ITV [112], NUIG [113]. These mechanisms have been widely used for flame and reactor modeling. The last three have been actively developed and tested in recent years.

The comparison focuses on the predicted carbon mass fraction (CMF) of species involved in soot formation. Here, CMF is defined as the mass of carbon in a given species normalized by the total carbon mass in the gas mixture, which remains constant in the absence of soot formation. Initially, the CMF of methane is equal to 1, indicating that all carbon is stored in CH_4 at $t = 0$ in the studied shock tube. It should be noted that the CRECK mechanism used in this work does not include "BIN" species, except for BIN1.

Figure 15 shows the variability in the predicted CMF of CH_4, C_2H_2, and A2R5 across different reaction mechanisms. The CMF of CH_4 serves as a useful indicator of carbon flux from the fuel to intermediate species. C_2H_2 is the most abundant hydrocarbon during pyrolysis and plays a key role in the HACA mechanism for PAH growth beyond benzene, as well as in surface growth of

soot. A2R5 has been identified as important for soot inception, due to its low-aromaticity free edge, which readily reacts with σ-radicals and, if partially hydrogenated, can form localized π-radicals that enable combined covalent/stacked complex formation [114].

As shown in the inset of Figure 15a, the CRECK mechanism predicts the highest CH_4 conversion up to 1 ms, but this trend reverses at longer residence times, where KAUST predicts the lowest CMF. ABF and NUIG underpredict the methane conversion rate by nearly 10% of the initial carbon compared to the other mechanisms. As expected, the majority (40–60%) of the initial carbon is converted to C_2H_2 by the end of the simulation. In the inset of Figure 15b, all mechanisms direct more carbon toward C_2H_2 by 5 ms. CRECK predicts the highest C_2H_2 CMF up to 1 ms, after which NUIG gives the largest C_2H_2 CMF. This is attributed to NUIG's lack of aromatic and large hydrocarbon species, so it does not account for the conversion of C_2H_2 to PAHs.

The relative difference between the mechanisms is most pronounced for A2R5, spanning over an order of magnitude between ABF and Caltech. This aligns with previous findings that the uncertainty in the predicted concentration of gas-phase species increases with molecular size [115]. Since soot inception is described as the dimerization of PAHs, such discrepancies are amplified — a one-order-of-magnitude variation in monomer concentration can lead to a two-order-of-magnitude difference in dimer formation.
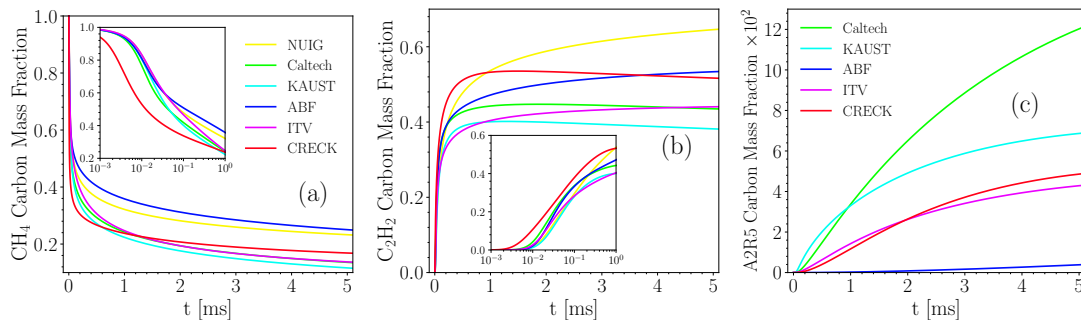
Figure 15: The carbon mass fraction of CH_4 (a), C_2H_2 (b), and A2R5 (c) at during pyrolysis of 10% CH_4-Ar predicted using different reaction mechanisms. The insets provide a zoomed-in view of the early-time behavior

Omnisoot supports all standard reaction mechanisms through Cantera. However, soot simulations in this study were conducted using Caltech and KAUST mechanisms, as both include the designated soot precursors and yield high carbon fluxes to PAHs, resulting in soot yields and volume fractions that closely match experimental measurements. Although the ITV mechanism also meets these criteria, its large size (759 species and 7582 reactions) significantly increases the computational cost of parametric studies and simulations.

The pyrolysis of a 5% CH_4–Ar mixture was investigated using a constant pressure reactor (CPR) model over a post-shock temperature range $T_5 = 1800$–3000 K and a pressure range $P_5 = 4.7$–7.1 bar. Since P_5 was not specified for each experiment (characterized by a given T_5), we assumed a linear increase of P_5 with T_5 within the specified range [116]. The Caltech mechanism was used to describe gas-phase chemistry. Inception and PAH adsorption rates were adjusted using η_{inc} and η_{ads}, respectively, to match the predicted carbon yield at $t = 1.5$ ms with light extinction measurements at $\lambda = 632$ nm over the studied T_5 and P_5 ranges [116]. The measured carbon yield (CY) was retrieved from the reported product CY×E(m). There are uncertainties in CY calculated using this technique due to variability in E(m). It is common to use the E(m) of mature soot, which may not be accurate for soot particles formed in a shock tube over short residence times (≈ 2 ms). E(m) increases significantly with particle size, composition, and maturity. For example, E(m) varies from 0.05 to 0.25 as the primary particle diameter grows to 20 nm within 1.6 ms during acetylene pyrolysis. However, there remains a substantial gap in our quantitative understanding of evolving E(m) values for soot. We considered the reported variability of E(m) in the literature, ranging from 0.174 [117] to 0.37 [118].The pyrolysis of a 5% CH_4–Ar mixture was investigated using a constant pressure

reactor (CPR) model over a post-shock temperature range $T_5 = 1800$–3000 K and a pressure range $P_5 = 4.7$–7.1 bar. Since P_5 was not specified for each experiment (characterized by a given T_5), we assumed a linear increase of P_5 with T_5 within the specified range [116]. The Caltech mechanism was used to describe gas-phase chemistry. Inception and PAH adsorption rates were adjusted using η_{inc} and η_{ads}, respectively, to match the predicted carbon yield at $t = 1.5$ ms with light extinction measurements at $\lambda = 632$ nm over the studied T_5 and P_5 ranges [116]. The measured carbon yield (CY) was retrieved from the reported product CY$\times$E(m). There are uncertainties in CY calculated using this technique due to variability in E(m). It is common to use the E(m) of mature soot, which may not be accurate for soot particles formed in a shock tube over short residence times (≈ 2 ms). E(m) increases significantly with particle size, composition, and maturity. For example, E(m) varies from 0.05 to 0.25 as the primary particle diameter grows to 20 nm within 1.6 ms during acetylene pyrolysis. However, there remains a substantial gap in our quantitative understanding of evolving E(m) values for soot. We considered the reported variability of E(m) in the literature, ranging from 0.174 [117] to 0.37 [118].

A parametric study was conducted on η_{inc} and η_{ads} using a grid search approach. Each factor was varied across 11 logarithmically spaced values from 10^{-4} to 1, resulting in 99 simulation cases per data point (792 simulations total). Combinations of η_{inc} and η_{ads} were ranked by the average relative error across all data points to identify the set minimizing the carbon yield prediction error. Figure 16 shows a heat map of the mean relative error, normalized by the maximum value, for the Reactive Dimerization model. The largest error occurs for the combination of maximum inception ($\eta_{inc} = 1$ or $\log_{10}(\eta_{inc}) = 0$) and minimum adsorption ($\eta_{ads} = 10^{-4}$ or $\log_{10}(\eta_{ads}) = -4$). The region of lowest normalized error (less than 5%) is outlined in blue and includes a broad set of adjustment factor combinations that accurately predict carbon yield but may affect predicted soot morphology.To better understand these effects, we adopted a multi-step approach: (i) simulations without soot were performed to isolate gas-phase chemistry and C_2H_2 formation; (ii) inception models were optimized using equal adjustment factors $\eta_{inc} = \eta_{ads}$; and (iii) separate optimizations were performed for minimum adsorption ($\eta_{ads} = 10^{-4}$) and minimum inception ($\eta_{inc} = 10^{-4}$), denoted as *Min Ads*.
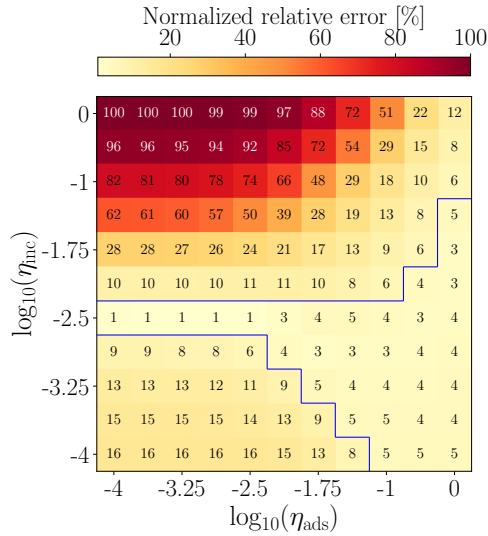

Figure 16: The relative error of carbon yield normalized by the maximum value at t=1.5 ms for 5% CH_4 obtained using Caltech mechanism and Reactive Dimerization

.

Figure 17a shows the carbon mass fraction (CMF) of soot precursors (individual PAHs and total) and C_2H_2 at 1.5 ms across the studied temperature range, with the soot model deactivated. While

PAH precursors exhibit a bell-shaped profile, the CMF of C_2H_2 increases linearly with temperature and plateaus near 85% at $T_5 \approx 2400$ K. Among the considered PAHs, A2, A2R5, and A4R5 account for most of the carbon and are likely major contributors to soot inception and surface growth. The significant variation in PAH CMF highlights the impact of precursor selection on inception flux, surface growth rates, and their temperature sensitivity. Figure 18 illustrates the effect of excluding five-membered ring PAHs (A2R5, A3R5, and A4R5) from the soot precursors on the carbon yield (CY) and primary particle diameter (d_p). As expected, excluding these species leads to a substantial reduction in CY: a factor of 3 for Reactive Dimerization and a factor of 12 for EBridge Modified. The peak CY temperature remains nearly unchanged for EBridge Modified but shifts to 2100 K for other inception models. The impact on d_p is less pronounced, showing a decrease for Reactive Dimerization and a slight increase for other models in the 2100–2500 K range.
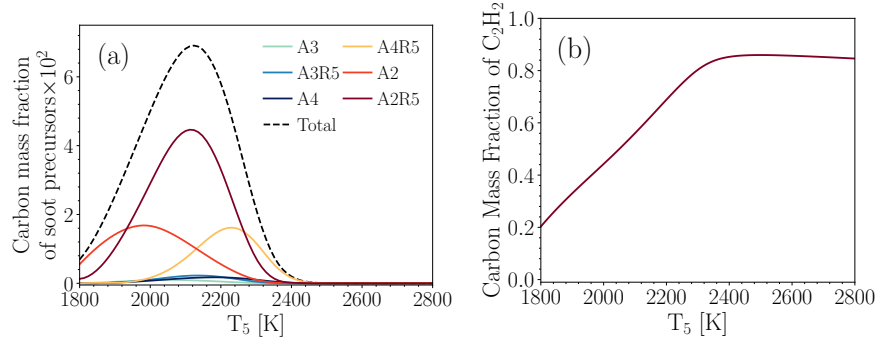
Figure 17: The bell-shape temperature profile of carbon mass fraction of soot precursors (A2 and larger) combined (a) and C_2H_2 (b) at t=1.5 ms during pyrolysis of 5% (red line) and 10% CH_4-Ar (green line) obtained using CPR model with Caltech mechanism without considering soot
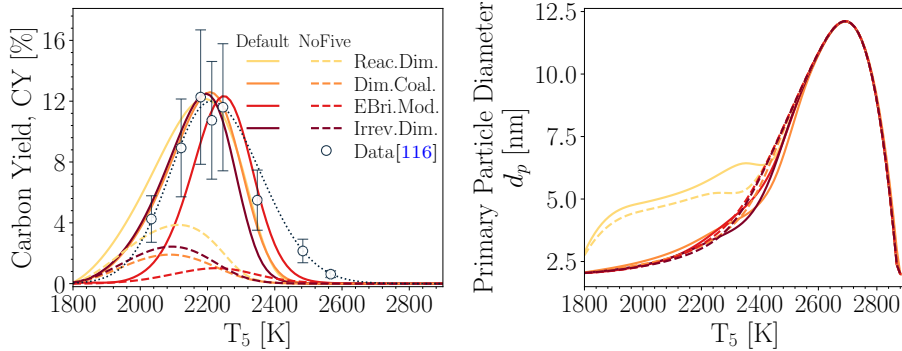
Figure 18: The soot carbon yield, CY at t=1.5 ms (a) and primary particle diameter, d_p (b) obtained using the default soot precursors listed in Table 1 (denoted by solid line and labeled as "Default"") compared with the same results when five-membered ring PAHs excluded from soot precursors (denoted by dashed line and labeled as "NoFive"). Both cases were obtained using Caltech mechanism and the same equal adjustment factors. The dashed line was added to show the trend in the measurements [116].

Next set of simulations were conducted by using equal adjustment factors ($\eta_{inc} = \eta_{ads}$) to minimize the prediction error of soot carbon yield. Figure 19 compares CY and d_p from various inception models with experimental extinction data [116]. A skew exponential curve (black dotted line) was fitted to highlight the CY trend and its peak near 12%. Soot CY follows a bell-shaped profile similar to that of soot precursors, as inception flux and mass growth directly depend on precursor concentrations. Reactive Dimerization predicts higher CY at lower temperatures, while EBridge Modified

38

shifts the peak to higher temperatures due to a different temperature dependency—primarily governed by PAH dehydrogenation via an Arrhenius rate law, in contrast to physical PAH collisions in other models. The predicted d_p increases with T_5, reaching a maximum of 12.5 nm at 2700 K, where yield is minimal ($\approx 10^{-7}$), and then drops to the model's minimum allowed value of 2 nm. Figure 20a shows that the total number of primary particles (N_{pri}) peaks at $\approx$ 2200 K, aligning with the peak in carbon yield. This is expected since N_{pri} depends solely on the inception flux, which is highest when PAH concentrations peak. Increased coagulation rates reduce the number of agglomerates (N_{agg}) in the 2000–2500 K range. The coagulation characteristic time depends on N_{agg} and β, which is temperature dependent. Reactive Dimerization yields the fewest particles (N_{pri} and N_{agg}) because more precursors are directed toward surface growth. Consequently, the number of primary particles per agglomerate (n_p) is lowest for Reactive Dimerization. Differences between inception models are more evident in n_p than in d_p, influencing predicted particle morphology. These differences become more pronounced at longer residence times. For instance, Dimer Coalescence predicts a more ramified agglomerate ($n_p = 38$) compared to Reactive Dimerization ($n_p = 12$). Additional morphological data could help constrain inception and surface growth rates in soot models.
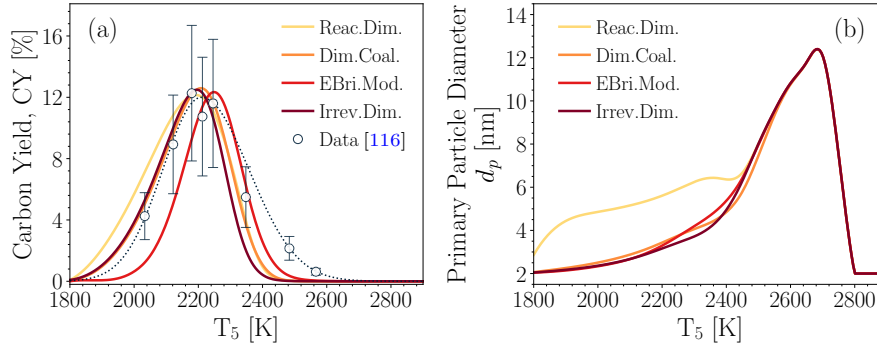

Figure 19: The bell-shape temperature profile of soot carbon yield at t=1.5 ms (a) and increasing primary particle diameter, d_p obtained using Caltech mechanism and different inception models optimized using equal adjustment factors to minimize the prediction with extinction measurements [116]. The dashed line was added to show the trend in the measurements.
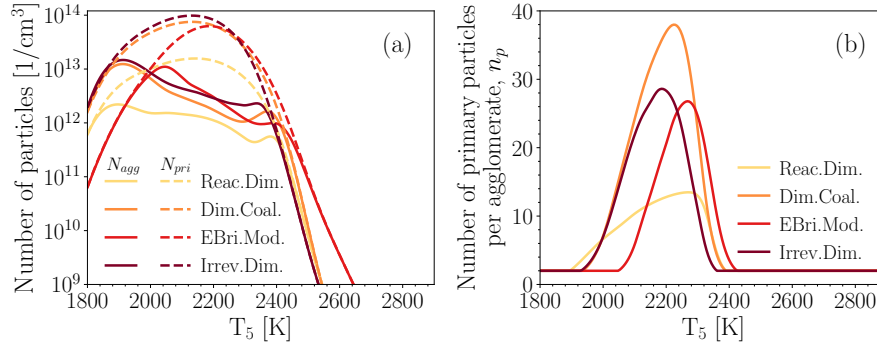

Figure 20: The temperature dependence of total number of agglomerates, N_{agg} (a), number of primary particles per agglomerate, n_p (b) at t=1.5 ms obtained using Caltech mechanism and different inception models optimized using equal adjustment factors to minimize the prediction with extinction measurements [116].

The differences of inception models in prediction of d_p is overall negligible except for Reactive

Dimerization, which predicts a larger d_p in T_5 <2500. The d_p trends can be better understood by examining Equation(24) indicating that d_p is proportional of the third-root of C_{tot}/N_{pri}. C_{tot} describes total carbon mass converted to soot through inception and surface growth while N_{pri} is only determined by inception flux. As a result, d_p is controlled by the ratio of surface growth (HACA and PAH adsorption) rate to inception flux. The ratio of carbon mass gained up to 1.5 ms by each pathway to the total soot carbon mass is calculated and shown in Figure 21. PAH adsorption is the dominant soot mass growth pathway for Reactive Dimerization in T_5 <2000 K (Figure 21-a) that results in larger C_{tot}/N_{pri} and d_p values, but inception is dominant for the other inception models. The carbon mass fraction of inception decreases with temperature for all inception models leading to higher d_p values up to 2700 K and it increases afterwards that changes d_p trends.
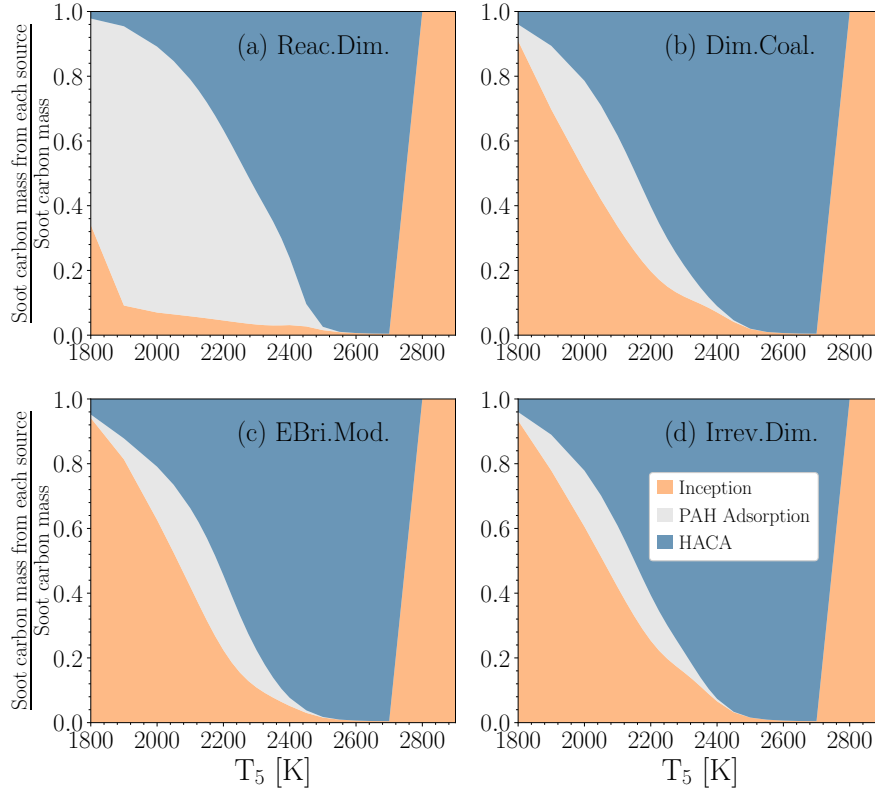
Figure 21: The soot carbon mass from inception, PAH adsorption and HACA normalized by total soot carbon mass at t=1.5 ms for 5% in Ar obtained using Caltech mechanism and different inception models calibrated to minimize the prediction with extinction measurements [116].

Figure 22 shows that optimizing models with minimum η_{inc} and η_{ads} yields similar CY predictions across inception models, except EBridge Modified, which shifts slightly toward higher temperatures. The minimum adsorption case has a higher peak and narrower profile compared to the minimum inception case. Figure 22 demonstrates the variation in d_p among the inception models with the minimum inception (solid line) mode compared to the minimum adsorption (dashed line) that show negligible sensitivity to the inception model. In the minimum inception mode, the majority of soot mass comes from PAHs, so d_p shows a bell-shape profile with a peak close to the temperature of CMF of precursors (dashed line in Figure 17). Reactive Dimerization has the largest variation at the peak from 2 to 21 nm for the minimum inception and adsorption, respectively. The global adjustment factors were used to alter the contribution of precursors to inception and surface growth without changing the internal rate constants of inception models. A close agreement was achieved between the predicted and measured carbon yield in different modes of inception and PAH adsorption that

can result in different soot morphology. Characterizing primary particle size in the experiment can reduce the uncertainty in the model and restrict the range of expected inception and surface growth rate and highlight the need to account for missing pathways and phenomena involved in soot yield and morphology.
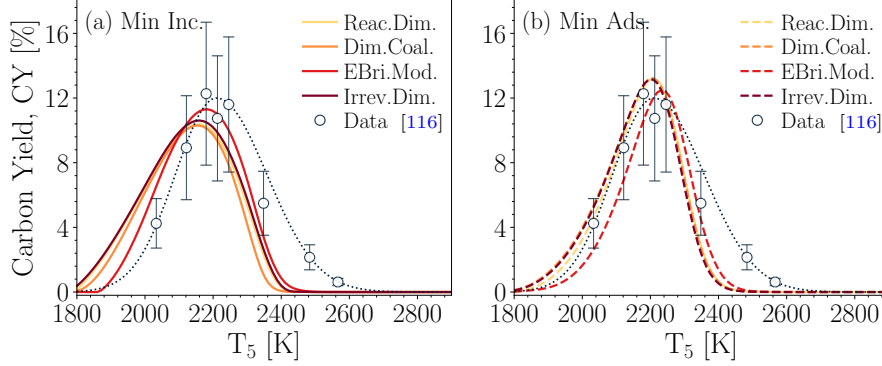

Figure 22: The comparison of soot carbon yield at t=1.5 ms when the minimum inception (a) and the minimum PAH adsorption (b) adjustment factors were applied to minimize the prediction error compared to measurements [116] for 5% CH_4-Ar obtained using Caltech mechanism and different inception models.
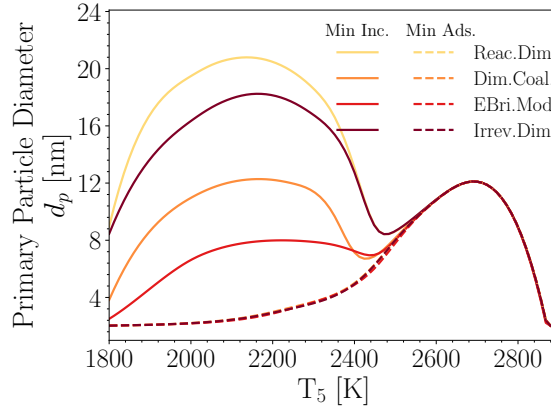
Figure 23: The comparison of mean primary particle, d_p at t=1.5 ms when the minimum inception (solid lines) and adsorption (dashed lines) were applied to minimized the prediction error compared to measurements [116] for 5%-Ar obtained using Caltech mechanism and different inception models.

4.1 Ethylene pyrolysis in a flow reactor

The plug flow reactor (PFR) model was used to simulate the pyrolysis of 0.6% C_2H_4–N_2 in a 1.4 m-long, 16 mm-diameter flow reactor. Figure 24 shows the axial temperature profile used in the simulations. The maximum temperature, T_{max} = 1673 K, was imposed on the model based on thermocouple measurements reported by Mei et al. [119] for various flow rates along the reactor centerline. The temperature increases from 300 K at the reactor inlet to the hot zone, where it reaches within 10% of T_{max}. The length of the hot zone varies with flow rate due to advection, ranging from 0.71 m at Q = 8 L/min to 0.76 m at Q = 12 L/min. Near the reactor outlet, the temperature drops to approximately 650 K.

The inception and PAH adsorption adjustment factors were varied to match the predicted particle size distribution (PSD) with experimental measurements at the reactor exit for flow rates of 8.5, 11,

and 12 L/min, as shown in Figure 25. The parametric analysis revealed that each inception model requires a unique set of adjustment factors to minimize the PSD prediction error across different flow rates. The KAUST mechanism [110] was used to describe gas-phase chemistry, as it provided better agreement with the measured PSDs than the Caltech mechanism.

A bimodal size distribution can be observed for Q=8 L/min (Figure 25-a) that was attributed to the continuous inception [97]. The comparison of simulations with measurements reveals different temperature dependence of inception models. Irreversible Dimerization and Dimer Coalescence (irreversible inception models) capture the bimodality of PSD in good agreement with the measurements, but the other two models predict a nearly unimodal PSD. The number concentration of the first section is lower by more than three orders of magnitude for Reactive Dimerization and EBridge Modified indicating the lack of active inception at the sampling location due the temperature drops near the end of reactor that suppresses soot inception.

All inception models capture the disappearance of the PSD shoulder at flow rates of 11 and 12 L/min. In these cases, the shorter particle residence time limits coagulation, preventing formation of a second peak. However, Reactive Dimerization and EBridge Modified still underpredict the number concentration of nascent particles by approximately one order of magnitude compared to the irreversible models.

Figure 25 also presents the axial evolution of the total number concentration of agglomerates (N_{agg}). Predictions from all models agree closely up to $z \approx 1.1$ m, corresponding to the end of the hot zone. Beyond this point, N_{agg} continues to increase for the irreversible models, which allow soot inception to proceed in cooler downstream regions. These models agree well with experimental data at 8 and 11 L/min but tend to overpredict N_{agg} at 12 L/min.

As shown in Figure 27, soot inception flux rises sharply as the gas enters the hot zone. The axial location where the flux exceeds 10^7 cm^{-3} s^{-1} is similar across all inception models, as it is primarily determined by PAH chemistry. However, this location shifts downstream with increasing flow rate due to reduced residence time. Within the hot zone, differences among the inception models are minimal. Outside the hot zone, Irreversible Dimerization and Dimer Coalescence maintain high inception flux, while Reactive Dimerization and EBridge Modified predict a rapid decrease of more than three orders of magnitude due to cooling. Figure 28 demonstrates the contribution of each pathway to total carbon mass of soot along the reactor that elucidate the link between the balance of inception and surface growth with particle morphology. The relative strength of inception decreases from 100% to less than 5% by z=1.1 m for all inception models leading to a gradual increase of d_p and d_m. Irreversible Dimerization and Dimer Coalescence predict an increase in contribution of inception that resulting in the decline of d_p while Reactive Dimerization and EBridge Modified predict a nearly constant d_p.

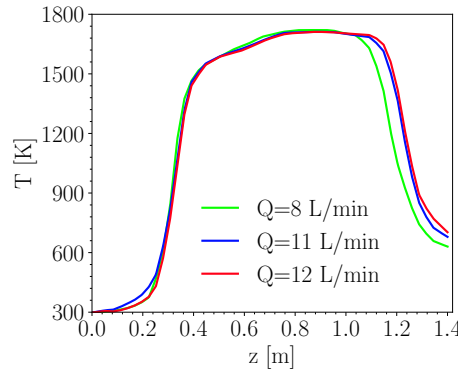
Figure 24: The centerline temperature along the reactor for Q=8, 11, and 12 L/mi interpolated from the thermocouple measurements [119]. The yellow area represent the region with temperature larger than 1200 K.
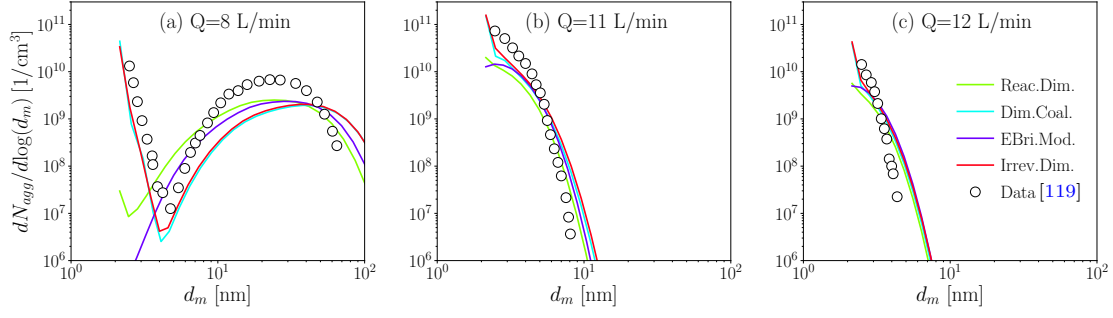
Figure 25: The particle size distribution at the end of PFR for Q=8.5 (a), 11 (b), and 12 L/min (c) obtained using KAUST mechanism and different inception models calibrated to match the predictions with measurement [119].
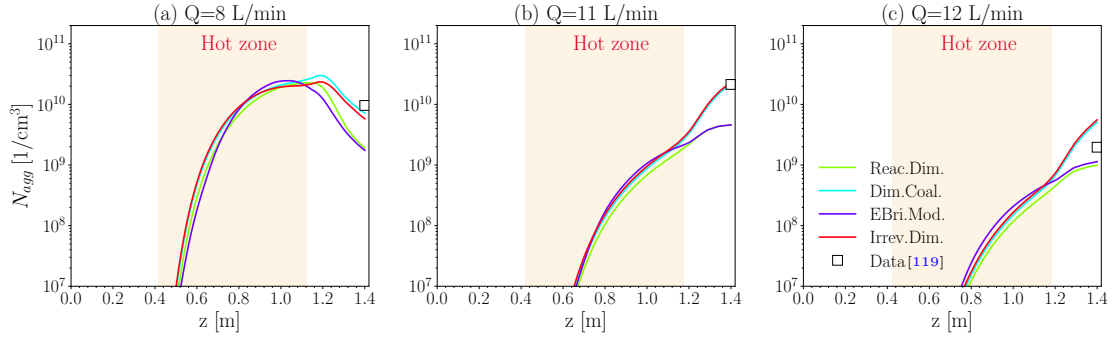

Figure 26: The total number of agglomerates along the PFR for Q=8.5 (a), 11 (b), and 12 L/min (c) obtained using KAUST mechanism and different inception models compared with data [119].
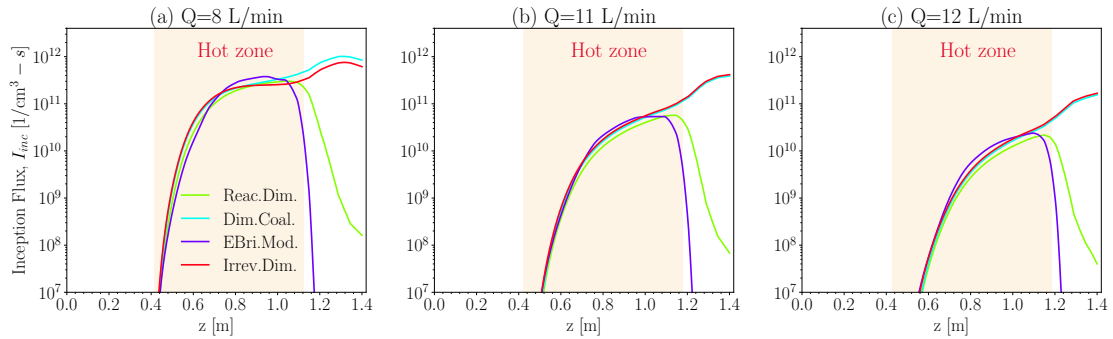

Figure 27: The soot inception flux along the PFR for Q=8.5 (a), 11 (b), and 12 L/min (c) obtained using KAUST mechanism and different inception models.
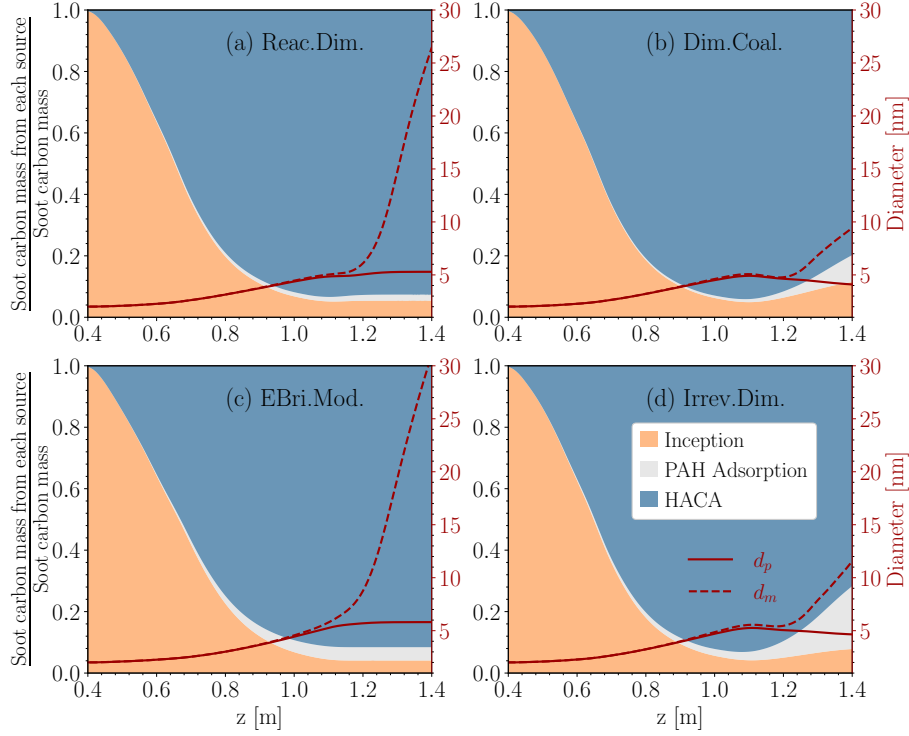
Figure 28: The soot carbon mass from inception, PAH adsorption and HACA normalized by total soot carbon mass for Q=8.5 L/min along with primary particle d_p, and mobility, d_m diameter obtained using KAUST mechanism and different inception models.

4.2   Ethylene oxidation in a partially-stirred reactor

Manzello et al. [120] utilized a well-stirred reactor (WSR) connected to a flow reactor to study soot formation during ethylene oxidation at equivalence ratios, $\phi = 1.9$, 2.0, and 2.1, and provided PSD measurements at the end of flow reactor using nano-differential mobility analyzer (Nano-DMA). The WSR had the same size of the reactor used by Manzello et al. [120] and explained in Sec.3.5. The flow reactor is 70 cm long with an inner diameter of 5.1 cm. A coupled PSR-PFR reactor model of omnisoot was used to simulate soot formation during the combustion and flow evolution in the device. The nominal residence time, τ of flow in the PSR is 11 ms [120]. The reactants are assumed to enter PSR at 300 K with an inlet mass flow rate, $\dot{m}_{in} = \rho V / \tau$ where ρ was calculated at reactor temperature of 1723 K suggested by Lenhert and Manzello [121]. The PFR is assumed to be adiabatic. The calculated average axial velocity in the PFR is 14.5 m/s close to the values suggested by Manzello et al. [120]. KAUST mechanism was used to describe gas chemistry.

The inception and PAH adsorption adjustment factors were varied for each PAH growth model to match the predicted PSD with the measurements as closely as possible for all three ϕs. As shown in Figure 29, all inception models capture the peak number concentration and the unimodal shape of the PSD, which indicates that particle inception has ceased, and coagulation is the dominant mechanism for agglomerate size growth. As reported in Table 5, the geometric mean mobility diameter, $d_{m,g}$ and the geometric mobility standard deviation, $\sigma_{m,g}$ obtained using all inception models are in good agreement with the values calculated from the measured PSD [120]. As it can be seen in Figure 29-(a) & (b), the spread of predicted PSD is narrower than that of measurements for ϕ=1.9 and 2.1, which corresponds to under-prediction of $\sigma_{m,g}$ for these equivalence ratios.
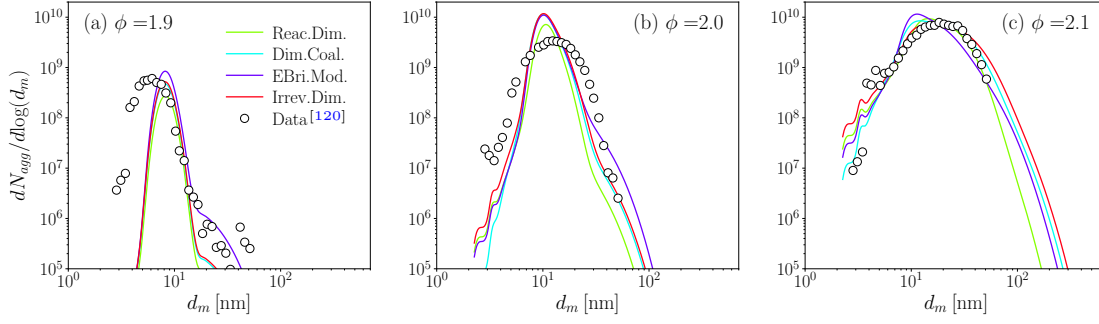
Figure 29: The particle size distribution at the end of PFR for ϕ=1.9 (a), 2.0 (b), and 2.1 (c) obtained using KAUST mechanism and different inception models calibrated to match the predictions with measurement [120].

Table 5: The geometric mean mobility diameter, $d_{m,g}$, and the geometric mobility standard deviation, $\sigma_{m,g}$ obtained using different inception models compared with the value calculated from the measured PSD [120]

	ϕ =1.9		ϕ =2.0		ϕ =2.1	
	$d_{m,g}$ [nm]	$\sigma_{m,g}$	$d_{m,g}$ [nm]	$\sigma_{m,g}$	$d_{m,g}$ [nm]	$\sigma_{m,g}$
Data [120]	6.04	1.25	12.40	1.49	17.66	1.64
Reactive Dimerization	8.27	1.14	11.10	1.21	16.88	1.58
Dimer Coalescence	8.18	1.14	10.76	1.24	16.99	1.68
EBridge Modified	8.27	1.15	11.02	1.27	14.56	1.58
Irreversible Dimerization	8.19	1.14	10.96	1.25	18.44	1.78

All inception models underpredict the number concentration of small particles (d_m <6 nm) at ϕ=1.9. The discrepancy decreases for ϕ=2 and the model predictions align well with the measurements. The number concentration of the smallest measured particle ($\approx$2 nm) is less affected by equivalence ratio compared to the numerical results. This suggests a stronger sensitivity of the PAH production rate to variation of ϕ from 1.9 to 2.1, which directly impacts soot inception flux. The strong similarity of profiles of acenaphthylene (A2R5) mole fraction and soot inception along the reactor shown in Fig .30 highlights the dominant role of PAH chemistry on soot inception. Another important observation is that A2R5 mole fraction is not affected by the employed inception model. One order of magnitude increase in peak A2R5 mole fraction due to the change of ϕ from 1.9 to 2.1 is amplified leading to two orders of magnitude increase in inception flux.

As shown in Figure 31, primary particle diameter, d_p along the flow reactor is nearly the same for all inception models at ϕ=1.9, but the difference becomes noticeable for higher ϕ values. Reactive Dimerization predicts the largest final d_p because it directs more PAH mass to surface growth rather than inception, which is consistent with lower peak number concentration observed in Figure 29. d_p rapidly decreases at the beginning of the reactor flow due to the rise in the production of incipient particles (spherical particles with diameter of 2 nm) that lowers the mean d_p of particles. Then, d_p increases by surface growth towards the end of reactor. The final d_p slightly increases with ϕ, but its range is similar for ϕ values. As shown in Figure 32, soot volume fraction however is very

sensitive to equivalence ratio, which can be explained by the strong effect of equivalence ratio on PAH production, inception flux, and number of particles. The analysis of surface growth rates at end of PFR revealed that more than 95% of soot mass is gained through HACA. Figure 33 illustrates the coupling between number concentration of agglomerates, N_{agg} and HACA growth rate and their change due to equivalence ratio.
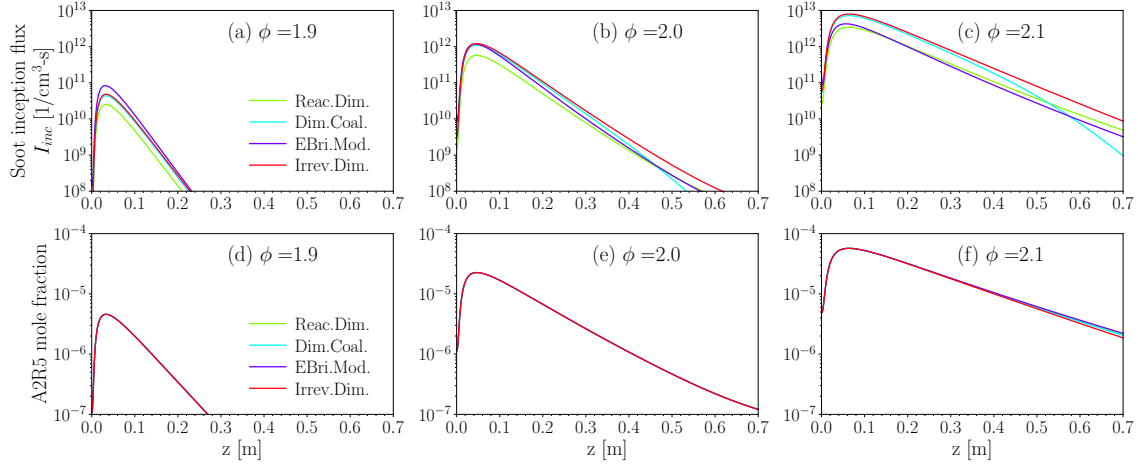

Figure 30: The soot inception flux, I_{inc} and acenaphthylene, A2R5 mole fraction along the PFR for ϕ=1.9 (a,d), 2.0 (b,e), and 2.1 (c,f) obtained using KAUST mechanism and different inception models calibrated to match the predictions with measurement [120].

Figure 31: The primary particle diameter, d_p along the PFR for ϕ=1.9 (a), 2.0 (b), and 2.1 (c) obtained using KAUST mechanism and different inception models calibrated to match the predictions with measurement [120].
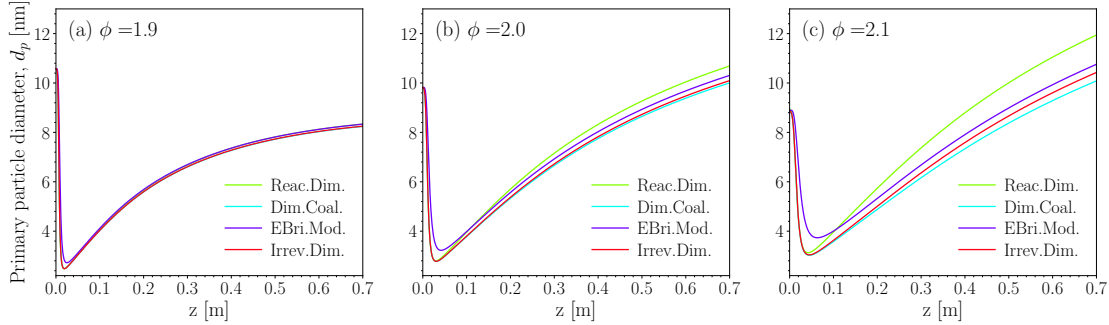
Figure 32: The soot volume fraction along the PFR for ϕ=1.9 (a), 2.0 (b), and 2.1 (c) obtained using KAUST mechanism and different inception models calibrated to match the predictions with measurement [120].
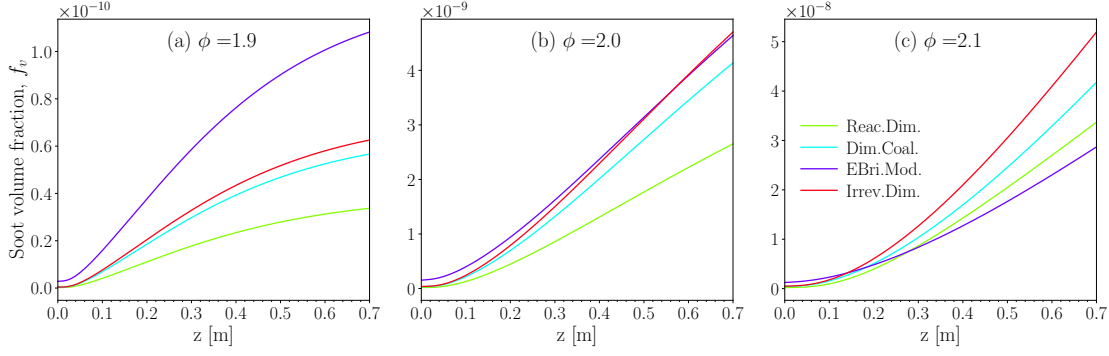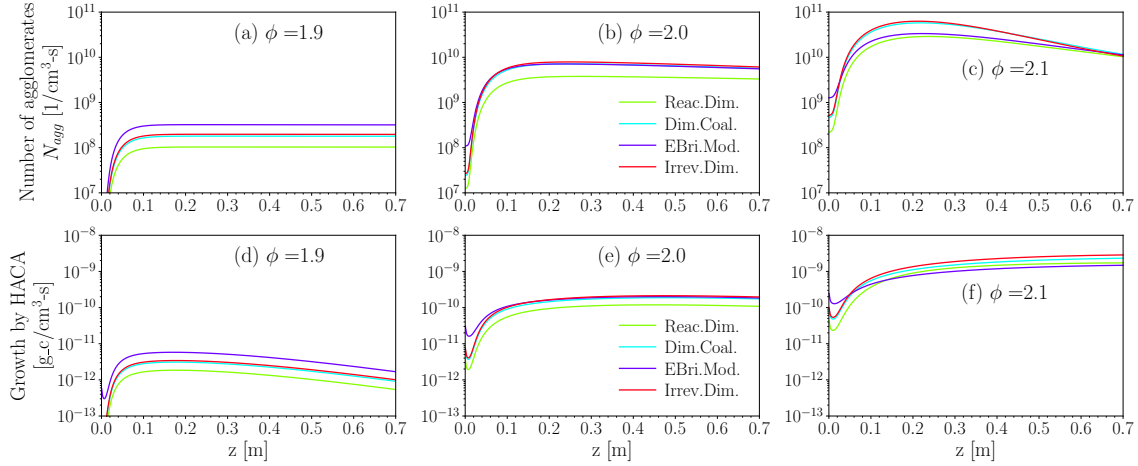

Figure 33: The number of agglomerates, N_{agg} and the rate of carbon addition by HACA along the PFR for ϕ=1.9 (a,d), 2.0 (b,e), and 2.1 (c,f) obtained using KAUST mechanism and different inception models calibrated to match the predictions with measurement [120].

5   Conclusion

This work presents Omnisoot as a robust computational tool built on Cantera to simulate soot formation coupled with gas-phase chemistry across various combustion and pyrolysis scenarios. Omnisoot integrates four reactor models, two aerosol dynamics models, and four inception and surface growth models, providing a comprehensive platform for analyzing uncertainties in predicting soot yield and morphology originating from chemical kinetics, inception processes, and surface growth rates. The tool was employed to elucidate differences among inception models in shock tubes, flow reactors, and well-stirred reactors.

Global adjustment factors were applied to inception and surface growth rates to accurately reproduce experimental data for each target scenario across a range of parameters, including temperature, pressure, composition (equivalence ratio), and flow rates. The performance of inception models was evaluated based on soot yield, morphology, size distribution, inception and surface growth rates, and carbon mass source analysis. Although different inception models predicted similar carbon yields

that closely matched experimental observations, they produced varying morphological characteristics. This highlights the importance of characterizing soot morphology to better constrain inception flux and surface growth rate predictions.

Simulations of ethylene pyrolysis in a flow reactor demonstrated the temperature sensitivity of inception models. Irreversible models (Irreversible Dimerization and Dimer Coalescence) effectively captured the bimodal particle size distribution resulting from high inception flux in the lower-temperature region near the reactor exit. However, the Reactive Dimerization and EBridge models generated nearly unimodal distributions due to their strong temperature dependence, causing a significant drop in inception flux in the same region.

The particle size distribution sampled at the outlet of a flow reactor downstream of a well-stirred reactor showed good agreement with experimental measurements across three equivalence ratios. Simulations indicated that active inception and surface growth primarily occur at high temperatures within the well-stirred reactor and at the entrance region of the flow reactor, far upstream of the sampling location. Under these conditions, the particle size distribution, morphology, and inception flux predictions were largely consistent across all inception models, although notable differences were observed in soot volume fraction due to variations in predicted HACA growth rate

6 Acknowledgements

References

[1] Andrea D'Anna. Combustion-formed nanoparticles. *Proceedings of the Combustion Institute*, 32(1):593–613, 2009.

[2] Gunnar Myhre, Drew Shindell, and Julia Pongratz. Anthropogenic and natural radiative forcing. 2014.

[3] Paul JA Borm, Roel PF Schins, and Catrin Albrecht. Inhaled particles and lung cancer, part b: paradigms and risk assessment. *International journal of cancer*, 110(1):3–14, 2004.

[4] International Carbon Black Association et al. Carbon black user's guide. *available at www. carbon-black. org*, 2016.

[5] Verónica Palomares, Aintzane Goñi, Izaskun Gil De Muro, Iratxe De Meatza, Miguel Bengoechea, Igor Cantero, and Teófilo Rojo. Conductive additive content balance in li-ion battery cathodes: Commercial carbon blacks vs. in situ carbon from lifepo4/c composites. *J. Power Sources*, 195:7661–7668, 2010. ISSN 0378-7753.

[6] Tianyang Li, Christophe Rehmet, Yan Cheng, Yong Jin, and Yi Cheng. Experimental comparison of methane pyrolysis in thermal plasma. *Plasma Chemistry and Plasma Processing*, 37:1033–1049, 2017.

[7] Laurent Fulcheri, Vandad-Julien Rohani, Elliott Wyse, Ned Hardman, and Enoch Dames. An energy-efficient plasma methane pyrolysis process for high yields of carbon black and hydrogen. *International Journal of Hydrogen Energy*, 48(8):2920–2928, 2023.

[8] Shashank Reddy Patlolla, Kyle Katsu, Amir Sharafian, Kevin Wei, Omar E Herrera, and Walter Mérida. A review of methane pyrolysis technologies for hydrogen production. *Renewable and Sustainable Energy Reviews*, 181:113323, 2023.

[9] Soo-Jin Park, Min-Kang Seo, and Changwoon Nah. Influence of surface characteristics of carbon blacks on cure and mechanical behaviors of rubber matrix compoundings. *Journal of colloid and interface science*, 291(1):229–235, 2005.

[10] Ann Y Watson and Peter A Valberg. Carbon black and soot: two different substances. *AIHAJ-American Industrial Hygiene Association*, 62(2):218–228, 2001.

[11] C Russo, A Tregrossi, and A Ciajolo. Dehydrogenation and growth of soot in premixed flames. *Proceedings of the Combustion Institute*, 35(2):1803–1809, 2015.

[12] Madhu Singh and Randy L Vander Wal. Nanostructure quantification of carbon blacks. *C*, 5 (1):2, 2018.

[13] Randy L Vander Wal, Aleksey Yezerets, Neal W Currier, Do Heui Kim, and Chong Min Wang. Hrtem study of diesel soot collected from diesel particulate filters. *Carbon*, 45(1):70–77, 2007.

[14] Magín Lapuerta, Javier Barba, Anton D Sediako, Mohammad Reza Kholghy, and Murray J Thomson. Morphological analysis of soot agglomerates from biodiesel surrogates in a coflow burner. *Journal of Aerosol Science*, 111:65–74, 2017.

[15] Kiminori Ono, Kazuki Dewa, Yoshiya Matsukawa, Yasuhiro Saito, Yohsuke Matsushita, Hideyuki Aoki, Koki Era, Takayuki Aoki, and Togo Yamaguchi. Experimental evidence for the sintering of primary soot particles. *Journal of Aerosol Science*, 105:1–9, 2017.

[16] Jiangjun Wei, Yang Zeng, Mingzhang Pan, Yuan Zhuang, Liang Qiu, Taotao Zhou, and Yongqiang Liu. Morphology analysis of soot particles from a modern diesel engine fueled with different types of oxygenated fuels. *Fuel*, 267:117248, 2020.

[17] Hai Wang. Formation of nascent soot and other condensed-phase materials in flames. *Proc Combust Inst.*, 33:41–67, 2011. ISSN 15407489.

[18] Michael Frenklach and Hai Wang. Detailed modeling of soot particle nucleation and growth. In *Symposium (International) on Combustion*, volume 23, pages 1559–1566. Elsevier, 1991.

[19] Steffen Salenbauch, Alberto Cuoci, Alessio Frassoldati, Chiara Saggese, Tiziano Faravelli, and Christian Hasse. Modeling soot formation in premixed flames using an extended conditional quadrature method of moments. *Combustion and Flame*, 162(6):2529–2543, 2015.

[20] Pascale Desgroux, Alessandro Faccinetto, Xavier Mercier, Thomas Mouton, Damien Aubagnac Karkar, and Abderrahman El Bakali. Comparative study of the soot formation process in a "nucleation" and a "sooting" low pressure premixed methane flame. *Combustion and Flame*, 184:153–166, 2017.

[21] Yu Wang, Abhijeet Raj, and Suk Ho Chung. Soot modeling of counterflow diffusion flames of ethylene-based binary mixture fuels. *Combustion and Flame*, 162(3):586–596, 2015.

[22] Lei Xu, Fuwu Yan, Mengxiang Zhou, and Yu Wang. An experimental and modeling study on sooting characteristics of laminar counterflow diffusion flames with partial premixing. *Energy*, 218:119479, 2021.

[23] Mohammad Reza Kholghy, Armin Veshkini, and Murray John Thomson. The core–shell internal nanostructure of soot–a criterion to model soot maturity. *Carbon*, 100:508–536, 2016.

[24] Armin Veshkini, Seth B Dworkin, and Murray J Thomson. Understanding soot particle size evolution in laminar ethylene/air diffusion flames using novel soot coalescence models. *Combustion Theory and Modelling*, 20(4):707–734, 2016.

[25] J Houston Miller, Kermit C Smyth, and W Gary Mallard. Calculations of the dimerization of aromatic hydrocarbons: Implications for soot formation. In *Symposium (International) on Combustion*, volume 20, pages 1139–1147. Elsevier, 1985.

[26] Hassan Sabbah, Ludovic Biennier, Stephen J Klippenstein, Ian R Sims, and Bertrand R Rowe. Exploring the role of pahs in the formation of soot: Pyrene dimerization. *The Journal of Physical Chemistry Letters*, 1(19):2962–2967, 2010.

[27] Ali Naseri, M Reza Kholghy, Neil A Juan, and Murray J Thomson. Simulating yield and morphology of carbonaceous nanoparticles during fuel pyrolysis in laminar flow reactors enabled by reactive inception and aromatic adsorption. *Combustion and Flame*, 237:111721, 2022.

[28] Nazly E Sanchez, Alicia Callejas, Angela Millera, Rafael Bilbao, and Maria U Alzueta. Polycyclic aromatic hydrocarbon (pah) and soot formation in the pyrolysis of acetylene and ethylene: effect of the reaction temperature. *Energy & fuels*, 26(8):4823–4829, 2012.

[29] Sanghwan Cho, Seunghoon Lee, Wonnam Lee, and Sunho Park. Synthesis of primary-particle-size-tuned soot particles by controlled pyrolysis of hydrocarbon fuels. *Energy & Fuels*, 30(8): 6614–6619, 2016.

[30] Mohammad Reza Kholghy, Nick Anthony Eaves, Armin Veshkini, and Murray John Thomson. The role of reactive pah dimerization in reducing soot nucleation reversibility. *Proceedings of the Combustion Institute*, 37(1):1003–1011, 2019.

[31] Mohammad R Kholghy, Georgios A Kelesidis, and Sotiris E Pratsinis. Reactive polycyclic aromatic hydrocarbon dimerization drives soot nucleation. *Physical Chemistry Chemical Physics*, 20(16):10926–10938, 2018.

[32] Michael Frenklach and Alexander M Mebel. On the mechanism of soot nucleation. *Physical Chemistry Chemical Physics*, 22(9):5314–5331, 2020.

[33] Aamir D Abid, Joaquin Camacho, David A Sheen, and Hai Wang. Quantitative measurement of soot particle size distribution in premixed flames–the burner-stabilized stagnation flame approach. *Combustion and Flame*, 156(10):1862–1870, 2009.

[34] Guillaume Blanquart and Heinz Pitsch. A joint volume-surface-hydrogen multi-variate model for soot formation. *Combustion generated fine carbonaceous particles*, pages 437–463, 2009.

[35] Michael Frenklach. Reaction mechanism of soot formation in flames. *Physical chemistry chemical Physics*, 4(11):2028–2037, 2002.

[36] Jörg Appel, Henning Bockhorn, and Michael Frenklach. Kinetic modeling of soot formation with detailed chemistry and physics: laminar premixed flames of c2 hydrocarbons. *Combustion and flame*, 121(1-2):122–136, 2000.

[37] IT Woods and BS Haynes. Soot surface growth at active sites. *Combustion and flame*, 85 (3-4):523–525, 1991.

[38] Cameron J Dasch. The decay of soot surface growth reactivity and its importance in total soot formation. *Combustion and flame*, 61(3):219–225, 1985.

[39] Hope A Michelsen, Meredith B Colket, Per-Erik Bengtsson, Andrea D'anna, Pascale Desgroux, Brian S Haynes, J Houston Miller, Graham J Nathan, Heinz Pitsch, and Hai Wang. A review of terminology used to describe soot formation and evolution under combustion and pyrolytic conditions. *ACS nano*, 14(10):12470–12490, 2020.

[40] OI Obolensky, VV Semenikhina, AV Solov'Yov, and W Greiner. Interplay of electrostatic and van der waals forces in coronene dimer. *International Journal of Quantum Chemistry*, 107(6): 1335–1343, 2007.

[41] FS Lai, SK Friedlander, J Pich, and GM Hidy. The self-preserving particle size distribution for brownian coagulation in the free-molecule regime. *Journal of Colloid and Interface Science*, 39(2):395–405, 1972.

[42] Raymond D Mountain, George W Mulholland, and Howard Baum. Simulation of aerosol agglomeration in the free molecular and continuum flow regimes. *Journal of Colloid and Interface Science*, 114(1):67–81, 1986.

[43] Eirini Goudeli, Maximilian L Eggersdorfer, and Sotiris E Pratsinis. Coagulation of agglomerates consisting of polydisperse primary particles. *Langmuir*, 32:9276–9285, 2016. ISSN 0743-7463.

[44] Georgios A Kelesidis and Eirini Goudeli. Self-preserving size distribution and collision frequency of flame-made nanoparticles in the transition regime. *Proceedings of the Combustion Institute*, 38(1):1233–1240, 2021.

[45] Georgios A. Kelesidis, Eirini Goudeli, and Sotiris E. Pratsinis. Flame synthesis of functional nanostructured materials and devices: Surface growth and aggregation. *Proc Combust Inst .*, 36:29–50, 2017. ISSN 15407489.

[46] Georgios A Kelesidis and Sotiris E Pratsinis. A perspective on gas-phase synthesis of nanomaterials: Process design, impact and outlook. *Chemical Engineering Journal*, 421:129884, 2021.

[47] Georgios A. Kelesidis, Eirini Goudeli, and Sotiris E. Pratsinis. Morphology and mobility diameter of carbonaceous aerosols during agglomeration and surface growth. *Carbon*, 121: 527–535, 9 2017. ISSN 00086223.

[48] Andrei Kazakov and Michael Frenklach. Dynamic modeling of soot particle coagulation and aggregation: Implementation with the method of moments and application to high-pressure laminar premixed flames. *Combustion and flame*, 114(3-4):484–501, 1998.

[49] F Einar Kruis, Karl A Kusters, Sotiris E Pratsinis, and Brian Scarlett. A simple model for the evolution of the characteristics of aggregate particles undergoing coagulation and sintering. *Aerosol science and technology*, 19(4):514–526, 1993.

[50] Patrick T Spicer, Olivier Chaoul, Stavros Tsantilis, and Sotiris E Pratsinis. Titania formation by ticl4 gas phase oxidation, surface growth and coagulation. *J. Aerosol Sci.*, 33:17–34, 2002. ISSN 0021-8502.

[51] Aamir D Abid, Nicholas Heinz, Erik D Tolmachoff, Denis J Phares, Charles S Campbell, and Hai Wang. On evolution of particle size distribution functions of incipient soot in premixed ethylene–oxygen–argon flames. *Combustion and Flame*, 154(4):775–788, 2008.

[52] X Ma, CD Zangmeister, and MR Zachariah. Soot oxidation kinetics: a comparison study of two tandem ion-mobility methods. *The Journal of Physical Chemistry C*, 117(20):10723–10729, 2013.

[53] Joaquin Camacho, Changran Liu, Chen Gu, He Lin, Zhen Huang, Quanxi Tang, Xiaoqing You, Chiara Saggese, Yang Li, Heejung Jung, et al. Mobility size and mass of nascent soot particles in a benchmark premixed ethylene flame. *Combustion and Flame*, 162(10):3810–3822, 2015.

[54] Arto J Gröhn, Sotiris E Pratsinis, and Karsten Wegner. Fluid-particle dynamics during combustion spray aerosol synthesis of zro2. *Chemical Engineering Journal*, 191:491–502, 2012.

[55] Sotiris E Pratsinis. Simultaneous nucleation, condensation, and coagulation in aerosol reactors. *Journal of colloid and interface science*, 124(2):416–427, 1988.

[56] G Blanquart and H Pitsch. Analyzing the effects of temperature on soot formation with a joint volume-surface-hydrogen model. *Combustion and Flame*, 156(8):1614–1626, 2009.

[57] Michael Frenklach and Stephen J Harris. Aerosol dynamics modeling using the method of moments. *Journal of colloid and interface science*, 118(1):252–261, 1987.

[58] Stavros Tsantilis and Sotiris E Pratsinis. Soft-and hard-agglomerate aerosols made at high temperatures. *Langmuir*, 20(14):5933–5939, 2004.

[59] Peter R Lindstedt. Simplified soot nucleation and surface growth steps for non-premixed flames. In *Soot formation in combustion: mechanisms and models*, pages 417–441. Springer, 1994.

[60] Yun Xiong and Sotiris E Pratsinis. Formation of agglomerate particles by coagulation and sintering—part i. a two-dimensional solution of the population balance equation. *J. Aerosol Sci.*, 24:283–300, 1993. ISSN 0021-8502.

[61] MA Schiener and RP Lindstedt. Transported probability density function based modelling of soot particle size distributions in non-premixed turbulent jet flames. *Proceedings of the Combustion Institute*, 37(1):1049–1056, 2019.

[62] Themis Matsoukas and Sheldon K Friedlander. Dynamics of aerosol agglomerate formation. *Journal of Colloid and Interface Science*, 146(2):495–506, 1991.

[63] NA Fuchs. The mechanics of aerosol pergamon. *New York*, 1964.

[64] Yun Xiong and Sotiris E Pratsinis. Formation of agglomerate particles by coagulation and sintering—part i. a two-dimensional solution of the population balance equation. *Journal of Aerosol Science*, 24(3):283–300, 1993.

[65] Nick A Eaves, Qingan Zhang, Fengshan Liu, Hongsheng Guo, Seth B Dworkin, and Murray J Thomson. Coflame: A refined and validated numerical algorithm for modeling sooting laminar coflow diffusion flames. *Computer Physics Communications*, 207:464–477, 2016.

[66] Seth B Dworkin, Qingan Zhang, Murray J Thomson, Nadezhda A Slavinskaya, and Uwe Riedel. Application of an enhanced pah growth model to soot formation in a laminar coflow ethylene/air diffusion flame. *Combustion and Flame*, 158(9):1682–1695, 2011.

[67] Fengshan Liu, Ahmet E Karataş, Ömer L Gülder, and Mingyan Gu. Numerical and experimental study of the influence of co2 and n2 dilution on soot formation in laminar coflow c2h4/air diffusion flames at pressures between 5 and 20 atm. *Combustion and Flame*, 162(5):2231–2247, 2015.

[68] Andrea Nobili, Warumporn Pejpichestakul, Matteo Pelucchi, Alberto Cuoci, Carlo Cavallotti, and Tiziano Faravelli. Modeling soot particles as stable radicals: a chemical kinetic study on formation and oxidation. part ii. soot oxidation in flow reactors and laminar flames. *Combustion and Flame*, 243:112072, 2022.

[69] Alberto Cuoci, Alessio Frassoldati, Tiziano Faravelli, and Eliseo Ranzi. Opensmoke++: An object-oriented framework for the numerical modeling of reactive systems with detailed kinetic mechanisms. *Computer Physics Communications*, 192:237–264, 2015.

[70] Alberto Cuoci, Alessio Frassoldati, Tiziano Faravelli, and Eliseo Ranzi. A computational tool for the detailed kinetic modeling of laminar flames: Application to c2h4/ch4 coflow flames. *Combustion and Flame*, 160(5):870–886, 2013.

[71] David G. Goodwin, Harry K. Moffat, Ingmar Schoegl, Raymond L. Speth, and Bryan W. Weber. Cantera: An object-oriented software toolkit for chemical kinetics, thermodynamics, and transport processes. https://www.cantera.org, 2022. Version 2.6.0.

[72] Hope A Michelsen. Effects of maturity and temperature on soot density and specific heat. *Proceedings of the Combustion Institute*, 38(1):1197–1205, 2021.

[73] Kirk A Jensen, Jill M Suo-Anttila, and Linda G Blevins. Measurement of soot morphology, chemistry, and optical properties in the visible and near-infrared spectrum in the flame zone and overfire region of large jp-8 pool fires. *Combustion science and technology*, 179(12):2453–2487, 2007.

[74] Bonnie J McBride. *Coefficients for calculating thermodynamic and transport properties of individual species*, volume 4513. National Aeronautics and Space Administration, Office of Management . . . , 1993.

[75] Robert J Kee, Michael E Coltrin, Peter Glarborg, and Huayang Zhu. *Chemically reacting flow: theory, modeling, and simulation*. John Wiley & Sons, 2017.

[76] Skjalg E Haaland. Simple and explicit formulas for the friction factor in turbulent pipe flow. 1983.

[77] FP Berger and K-FF-L Hau. Mass transfer in turbulent pipe flow measured by the electrochemical method. *International Journal of Heat and Mass Transfer*, 20(11):1185–1194, 1977.

[78] George W Mulholland, RJ Samson, RD Mountain, and MH Ernst. Cluster size distribution for free molecular agglomeration. *Energy & Fuels*, 2(4):481–486, 1988.

[79] Georgios A Kelesidis and Sotiris E Pratsinis. Estimating the internal and surface oxidation of soot agglomerates. *Combustion and Flame*, 209:493–499, 2019.

[80] Jerôme Yon, A Bescond, and F-X Ouf. A simple semi-empirical model for effective density measurements of fractal aggregates. *Journal of Aerosol Science*, 87:28–37, 2015.

[81] Jenny Rissler, Maria E Messing, Azhar I Malik, Patrik T Nilsson, Erik Z Nordin, Mats Bohgard, Mehri Sanati, and Joakim H Pagels. Effective density characterization of soot agglomerates from various sources and comparison to aggregation theory. *Aerosol Science and Technology*, 47(7):792–805, 2013.

[82] Ganesan Narsimhan and Eli Ruckenstein. The brownian coagulation of aerosols over the entire range of knudsen numbers: Connection between the sticking probability and the interaction forces. *Journal of colloid and interface science*, 104(2):344–369, 1985.

[83] Antonio D'Alessio, AC Barone, R Cau, Andrea D'Anna, and P Minutolo. Surface deposition and coagulation efficiency of combustion generated nanoparticles in the size range from 1 to 10 nm. *Proceedings of the Combustion Institute*, 30(2):2595–2603, 2005.

[84] Hwa-Chi Wang and Gerhard Kasper. Filtration efficiency of nanometer-size aerosol particles. *Journal of Aerosol Science*, 22(1):31–41, 1991.

[85] Dingyu Hou, Diyuan Zong, Casper S Lindberg, Markus Kraft, and Xiaoqing You. On the coagulation efficiency of carbonaceous nanoparticles. *Journal of Aerosol Science*, 140:105478, 2020.

[86] Anna Ciajolo, Rosalba Barbella, Antonio Tregrossi, and Loretta Bonfanti. Spectroscopic and compositional signatures of pah-loaded mixtures in the soot inception region of a premixed ethylene flame. In *Symposium (International) on Combustion*, volume 27, pages 1481–1487. Elsevier, 1998.

[87] Christopher Betrancourt, Fengshan Liu, Pascale Desgroux, Xavier Mercier, Alessandro Faccinetto, Maurin Salamanca, Lena Ruwe, Katharina Kohse-Höinghaus, Daniel Emmrich, André Beyer, et al. Investigation of the size of the incandescent incipient soot particles in premixed sooting and nucleation flames of n-butane using lii, him, and 1 nm-smps. *Aerosol Science and Technology*, 51(8):916–935, 2017.

[88] Hope A Michelsen. Probing soot formation, chemical and physical evolution, and oxidation: A review of in situ diagnostic techniques and needs. *Proceedings of the Combustion Institute*, 36(1):717–735, 2017.

[89] Nikolaj A Fuchs, RE Daisley, Marina Fuchs, CN Davies, and ME Straumanis. The mechanics of aerosols, 1965.

[90] Jin Jwang Wu and Richard C Flagan. A discrete-sectional solution to the aerosol dynamic equation. *Journal of Colloid and interface Science*, 123(2):339–352, 1988.

[91] SH Park, SN Rogak, WK Bushe, JZ Wen, and MJ Thomson. An aerosol model to predict size and structure of soot particles. *Combustion Theory and Modelling*, 9(3):499–513, 2005.

[92] Michael Frenklach. New form for reduced modeling of soot oxidation: Accounting for multi-site kinetics and surface reactivity. *Combustion and Flame*, 201:148–159, 2019.

[93] BS Haynes and H Gg Wagner. The surface growth phenomenon in soot formation. *Zeitschrift für Physikalische Chemie*, 133(2):201–213, 1982.

[94] Stephen J Harris and Anita M Weiner. Chemical kinetics of soot particle growth. *Annual Review of Physical Chemistry*, 36(1):31–52, 1985.

[95] KH Homann. Formation of large molecules, particulates and ions in premixed hydrocarbon flames; progress and unresolved questions. In *Symposium (International) on Combustion*, volume 20, pages 857–870. Elsevier, 1985.

[96] Armin Veshkini. *Understanding Soot Particle Growth Chemistry and Particle Sizing Using a Novel Soot Growth and Formation Model*. University of Toronto (Canada), 2015.

[97] Bin Zhao, Zhiwei Yang, Murray V Johnston, Hai Wang, Anthony S Wexler, Michael Balthasar, and Markus Kraft. Measurement and numerical simulation of soot particle size distribution functions in a laminar premixed ethylene-oxygen-argon flame. *Combustion and Flame*, 133 (1-2):173–188, 2003.

[98] Joachim Happold, Horst-Henning Grotheer, and Manfred Aigner. Soot precursors consisting of stacked pericondensed pahs. *Combustion generated fine carbonaceous particles*, pages 275–285, 2009.

[99] K Olof Johansson, Tyler Dillstrom, Matteo Monti, Farid El Gabaly, Matthew F Campbell, Paul E Schrader, Denisia M Popolan-Vaida, Nicole K Richards-Henderson, Kevin R Wilson, Angela Violi, et al. Formation and emission of large furans and oxygenated hydrocarbons from flames. *Proceedings of the National Academy of Sciences*, 113(30):8374–8379, 2016.

[100] J Houston Miller, W Gary Mallard, and Kermit C Smyth. Intermolecular potential calculations for polycyclic aromatic hydrocarbons. *The Journal of Physical Chemistry*, 88(21):4963–4970, 1984.

[101] J Houston Miller. The kinetics of polynuclear aromatic hydrocarbon agglomeration in flames. In *Symposium (International) on Combustion*, volume 23, pages 91–98. Elsevier, 1991.

[102] Yoichiro Araki, Yoshiya Matsukawa, Yasuhiro Saito, Yohsuke Matsushita, Hideyuki Aoki, Koki Era, and Takayuki Aoki. Effects of carrier gas on the properties of soot produced by ethylene pyrolysis. *Fuel Processing Technology*, 213:106673, 2021.

[103] Binxuan Sun, Stelios Rigopoulos, and Anxiong Liu. Modelling of soot coalescence and aggregation with a two-population balance equation model and a conservative finite volume method. *Combustion and Flame*, 229:111382, 2021.

[104] A Tregrossi, A Ciajolo, and R Barbella. The combustion of benzene in rich premixed flames at atmospheric pressure. *Combustion and flame*, 117(3):553–561, 1999.

[105] Eirini Goudeli, Maximilian L Eggersdorfer, and Sotiris E Pratsinis. Coagulation–agglomeration of fractal-like particles: Structure and self-preserving size distribution. *Langmuir*, 31(4):1320–1327, 2015.

[106] M Reza Kholghy and Georgios A Kelesidis. Surface growth, coagulation and oxidation of soot by a monodisperse population balance model. *Combustion and Flame*, 227:456–463, 2021.

[107] Srinivas Vemury and Sotiris E Pratsinis. Self-preserving size distributions of agglomerates. *Journal of Aerosol Science*, 26(2):175–185, 1995.

[108] Scott Stouffer, Richard Striebich, Joseph Zelina, and Charles Frayne. Combustion particulates mitigation investigation using a well-stirred reactor. In *38th AIAA/ASME/SAE/ASEE Joint Propulsion Conference & Exhibit*, page 3723, 2002.

[109] G Blanquart, P Pepiot-Desjardins, and H Pitsch. Chemical mechanism for high temperature combustion of engine relevant fuels with emphasis on soot precursors. *Combustion and Flame*, 156(3):588–607, 2009.

[110] Yu Wang, Abhijeet Raj, and Suk Ho Chung. A pah growth mechanism and synergistic effect on pah formation in counterflow diffusion flames. *Combustion and flame*, 160(9):1667–1676, 2013.

[111] Chiara Saggese, Sara Ferrario, Joaquin Camacho, Alberto Cuoci, Alessio Frassoldati, Eliseo Ranzi, Hai Wang, and Tiziano Faravelli. Kinetic modeling of particle size distribution of soot in a premixed burner-stabilized stagnation ethylene flame. *Combustion and Flame*, 162(9):3356–3369, 2015.

[112] Maximilian Hellmuth, Raymond Langer, Anita Meraviglia, Joachim Beeckmann, and Heinz Pitsch. The role of c3 and c4 species in forming naphthalene in counterflow diffusion flames. *Proceedings of the Combustion Institute*, 40(1-4):105620, 2024.

[113] Long Zhu, Snehasish Panigrahy, Sarah N Elliott, Stephen J Klippenstein, Mohammadreza Baigmohammadi, A Abd El-Sabor Mohamed, Joshua W Hargis, Sulaiman Alturaifi, Olivier Mathieu, Eric L Petersen, et al. A wide range experimental study and further development of a kinetic model describing propane oxidation. *Combustion and Flame*, 248:112562, 2023.

[114] Jacob W Martin, Dingyu Hou, Angiras Menon, Laura Pascazio, Jethro Akroyd, Xiaoqing You, and Markus Kraft. Reactivity of polycyclic aromatic hydrocarbon soot precursors: implications of localized π-radicals on rim-based pentagonal rings. *The Journal of Physical Chemistry C*, 123(43):26673–26682, 2019.

[115] Yiqing Wang, Wang Han, Thorsten Zirwes, Antonio Attili, Liming Cai, Henning Bockhorn, Lijun Yang, and Zheng Chen. A systematic analysis of chemical mechanisms for ethylene oxidation and pah formation. *Combustion and Flame*, 253:112784, 2023.

[116] GL Agafonov, IV Bilera, PA Vlasov, IV Zhil'tsova, Yu A Kolbanovskii, VN Smirnov, and AM Tereza. Unified kinetic model of soot formation in the pyrolysis and oxidation of aliphatic and aromatic hydrocarbons in shock waves. *Kinetics and Catalysis*, 57:557–572, 2016.

[117] SC Lee and CL Tien. Optical constants of soot in hydrocarbon flames. In *Symposium (international) on combustion*, volume 18, pages 1159–1166. Elsevier, 1981.

[118] GL Agafonov, PA Vlasov, and VN Smirnov. Soot formation in the pyrolysis of benzene, methylbenzene, and ethylbenzene in shock waves. *Kinetics and Catalysis*, 52:358–370, 2011.

[119] Junyu Mei, Mengda Wang, Xiaoqing You, and Chung K Law. Quantitative measurement of particle size distributions of carbonaceous nanoparticles during ethylene pyrolysis in a laminar flow reactor. *Combustion and Flame*, 200:15–22, 2019.

[120] Samuel L Manzello, David B Lenhert, Ahmet Yozgatligil, Michael T Donovan, George W Mulholland, Michael R Zachariah, and Wing Tsang. Soot particle size distributions in a well-stirred reactor/plug flow reactor. *Proceedings of the Combustion Institute*, 31(1):675–683, 2007.

[121] David B Lenhert and Samuel L Manzello. Effects of benzene and naphthalene addition on soot inception in a well-stirred reactor/plug flow reactor. *Proceedings of the Combustion Institute*, 32(1):657–664, 2009.